A comprehensive model for right-left heart interaction under the influence of pericardium and baroreflex

YING SUN,[1] MAZEN BESHARA,[2] RICHARD J. LUCARIELLO,[2] AND SALVATORE A. CHIARAMIDA[2]

[1]*Department of Electrical and Computer Engineering, University of Rhode Island, Kingston, Rhode Island 02881; and* [2]*Division of Cardiology, Our Lady of Mercy University Hospital, Bronx, New York 10466*

Sun, Ying, Mazen Beshara, Richard J. Lucariello, and Salvatore A. Chiaramida. A comprehensive model for right-left heart interaction under the influence of pericardium and baroreflex. *Am. J. Physiol.* 272 (*Heart Circ. Physiol.* 41): H1499–H1515, 1997.—A phenomenological model of the cardiopulmonary circulation is developed with a focus on the interaction between the right heart and the left heart. The model predicts the hemodynamic consequences of changing circulatory parameters in terms of a broad spectrum of pressure and flow waveforms. Hemodynamics are characterized by use of an electrical analog incorporating mechanisms for transseptal pressure coupling, pericardial volume coupling, intrathoracic pressure, and baroreflex control of heart rate. Computer simulations are accomplished by numerically integrating 28 differential equations that contain nonlinear and time-varying coefficients. Validity of the model is supported by its accurate fit to clinical pressure and Doppler echocardiographic recordings. The model characterizes the hemodynamic waveforms for mitral stenosis, mitral regurgitation, left heart failure, right heart failure, cardiac tamponade, pulsus paradoxus, and the Valsalva maneuver. The wave shapes of pulmonary capillary wedge pressure under the above conditions are also accurately represented. Sensitivity analysis reveals that simulated hemodynamics are insensitive to most individual model parameters with the exception of afterload resistance, preload capacitances, intrathoracic pressure, contractility, and pericardial fluid volume. Baseline hemodynamics are minimally affected by transseptal coupling (up to 2%) and significantly affected by pericardial coupling (up to 20%). The model should be useful for quantitative studies of cardiopulmonary dynamics related to the right-left heart interaction under normal and disease conditions.

mathematical model; hemodynamics; cardiopulmonary circulation; septum; intrathoracic pressure; pulmonary wedge pressure; heart failure; mitral stenosis; mitral regurgitation; cardiac tamponade; pulsus paradoxus; Valsalva maneuver

RIGHT-LEFT HEART interaction has been recognized as an important factor in cardiovascular dynamics since the 19th century. Left heart failure (LHF) causes damming of blood in the pulmonary circulation, which in turn elevates afterload and preload of the right heart and can result in secondary right heart failure, a mechanism characterized by Hope's backward-failure hypothesis (16). The right heart supplies blood flow to the pulmonary circulation and indirectly controls preload of the left heart. Because pulmonary circulation and systemic circulation are in tandem, output of the right heart and the left heart must be equal at steady state, which is the basis for Mackenzie's forward-failure hypothesis (19). Although the etiology of pulmonary congestion can be explained by a blood volume shift from systemic to pulmonary circulation as a direct hemodynamic consequence of the right-left heart interaction (3), questions have been raised concerning the possible contribution to this process from other factors such as neurohormonal control (2).

The right heart and the left heart are also coupled by sharing the common septum and by competing for limited space in the pericardium. Whereas transseptal coupling is intrinsic to myocardial fiber structures, pericardial coupling is affected dynamically by all cardiac chambers and can be drastically accentuated by extrinsic factors such as pericardial effusion (5, 10). Although many studies (20, 24, 28, 36) have contributed in part to the understanding of the right-left heart interaction, our knowledge about the complex relationship between the right heart and the left heart is limited. In particular, quantitative characterization of the various mechanisms affecting the right-left heart interaction in intact circulation is lacking. Thus it should be useful to develop a computer model that simulates the cardiopulmonary system by integrating the various mechanisms for the right-left heart interaction.

Previous modeling work related to right-left heart coupling includes the following. Maughan et al. (20) characterized the interdependence between the right and the left ventricle in isolated canine hearts by use of an elastance compartment. Santamore and Burkhoff (24) applied the septal elastance model of Maughan et al. to assess hemodynamic consequences of ventricular interaction; however, their model did not include the pericardium. Hardy et al. (15) used a multicompartmental model to simulate pulsatile flow and gas transport and exchange. Beyar et al. (1) developed a comprehensive model to study the interaction between cardiac chambers and intrathoracic pressure. Most of these models were used to characterize certain causal relationships between circulatory variables and hemodynamic

consequences with the time variable removed; they did not provide hemodynamic waveforms. Some models (1, 15) were capable of generating baseline hemodynamic waveforms, but none of the models demonstrated the ability to simulate a broad spectrum of hemodynamic waveforms under various disease conditions. Nor did any of the aforementioned studies include the effects of neurohormonal control.

The purpose of the present study is to develop a computer model that provides a quantitative platform for studying hemodynamic waveforms and the various mechanisms for the right-left heart interaction under normal and disease conditions. The development of the model is dictated by the following considerations. *1*) The model is intended to be comprehensive in the sense that hemodynamics, respiratory effects, pericardial dynamics, and baroreflex control should be integrated into a single system. *2*) The model is intended to be phenomenological in the sense that not only time-invariant causal relationships but also time-varying hemodynamic waveforms should be accurately represented. *3*) The model is intended to be versatile in the sense that the same model can simulate a variety of conditions for normal and pathological physiology. *4*) The model is intended to provide knowledge for assessing left heart dynamics on the basis of right-sided measurements such as the pulmonary capillary wedge pressure. *5*) The model is intended to provide quantitative data for assessing how hemodynamic, transseptal, and pericardial coupling contribute to the right-left heart interaction.

Glossary

A_{av} Aortic valve area (cm^2)
A_{mv} Mitral valve area (cm^2)
A_{pv} Pulmonary valve area (cm^2)
A_{tv} Tricuspid valve area (cm^2)
b_{av} Bernoulli's resistance of aortic valve (mmHg·s^2·ml^{-2})
b_{mv} Bernoulli's resistance of mitral valve (mmHg·s^2·ml^{-2})
b_{pv} Bernoulli's resistance of pulmonary valve (mmHg·s^2·ml^{-2})
b_{tv} Bernoulli's resistance of tricuspid valve (mmHg·s^2·ml^{-2})
B Bernoulli's resistance (mmHg·s^2·ml^{-2})
e_{lv} Left ventricular elastance (mmHg/ml)
$\hat{e}_{lv}$ Effective e_{lv} with septal coupling (mmHg/ml)
e_{rv} Right ventricular elastance (mmHg/ml)
$\hat{e}_{rv}$ Effective e_{rv} with septal coupling (mmHg/ml)
E_{aa} Ascending aortic elastance (mmHg/ml)
E_{ca} Carotid arterial elastance (mmHg/ml)
E_{da} Descending aortic elastance (mmHg/ml)
E_{laa} Left atrial elastance amplitude (mmHg/ml)
E_{lab} Left atrial elastance baseline (mmHg/ml)
E_{lva} Left ventricular elastance amplitude (mmHg/ml)
E_{lvb} Left ventricular elastance baseline (mmHg/ml)
E_{pua} Pulmonary arterial elastance (mmHg/ml)
E_{puc} Pulmonary capillary elastance (mmHg/ml)
E_{puv} Pulmonary venous elastance (mmHg/ml)
E_{puv0} Pulmonary venous zero-volume elastance (mmHg/ml)
E_{pwa} Pulmonary arterial wedge elastance (mmHg/ml)
E_{pwc} Pulmonary capillary wedge elastance (mmHg/ml)
E_{pwv} Pulmonary venous wedge elastance (mmHg/ml)
E_{raa} Right atrial elastance amplitude (mmHg/ml)
E_{rab} Right atrial elastance baseline (mmHg/ml)
E_{rva} Right ventricular elastance amplitude (mmHg/ml)
E_{rvb} Right ventricular elastance baseline (mmHg/ml)
E_s Effective septal elastance (mmHg/ml)
E_{v0} Systemic venous zero-volume elastance (mmHg/ml)
g_{pw} Pulmonary wedge conductance (ml·s^{-1}·$mmHg^{-1}$)
IFSAP Inspiratory fall of systolic arterial pressure (mmHg)
k_{lr} Left-to-right ventricular pressure gain
k_{rl} Right-to-left ventricular pressure gain
K_{pc} Pericardial pressure coefficient (mmHg)
L_{aa} Ascending aortic inertance (mmHg·s^2·ml^{-1})
L_{av} Aortic valve inertance (mmHg·s^2·ml^{-1})
L_{ca} Carotid arterial inertance (mmHg·s^2·ml^{-1})
L_{da} Descending aortic inertance (mmHg·s^2·ml^{-1})
L_{mv} Mitral valve inertance (mmHg·s^2·ml^{-1})
L_{pua} Pulmonary arterial inertance (mmHg·s^2·ml^{-1})
L_{puc} Pulmonary capillary inertance (mmHg·s^2·ml^{-1})
L_{puv} Pulmonary venous inertance (mmHg·s^2·ml^{-1})
L_{pv} Pulmonary valve inertance (mmHg·s^2·ml^{-1})
L_{pwa} Pulmonary arterial wedge inertance (mmHg·s^2·ml^{-1})
L_{pwc} Pulmonary capillary wedge inertance (mmHg·s^2·ml^{-1})
L_{pwv} Pulmonary venous wedge inertance (mmHg·s^2·ml^{-1})
L_{tv} Tricuspid valve inertance (mmHg·s^2·ml^{-1})
L_{vc} Vena caval inertance (mmHg·s^2·ml^{-1})
L_v Systemic venous inertance (mmHg·s^2·ml^{-1})
p_{ao} Aortic pressure (mmHg)
p_{it} Intrathoracic pressure (mmHg)
P_{ita} Intrathoracic pressure amplitude (mmHg)
P_{itb} Intrathoracic pressure baseline (mmHg)
p_{la} Left atrial pressure (mmHg)
p_{lv} Left ventricular pressure (mmHg)
p_{pa} Pulmonary arterial pressure (mmHg)
p_{pc} Pericardial pressure (mmHg)
p_{pw} Pulmonary capillary wedge pressure (mmHg)
p_{ra} Right atrial pressure (mmHg)
p_{rv} Right ventricular pressure (mmHg)

$\dot{q}_{aa}$ Flow through ascending aorta (ml/s)
$\dot{q}_{av}$ Flow through aortic valve (ml/s)
$\dot{q}_{co}$ Flow through coronary artery (ml/s)
$\dot{q}_{da}$ Flow through descending aorta (ml/s)
$\dot{q}_{mv}$ Flow through mitral valve (ml/s)
$\dot{q}_{pua}$ Flow through pulmonary arteries (ml/s)
$\dot{q}_{puc}$ Flow through pulmonary capillaries
$\dot{q}_{puv}$ Flow through pulmonary veins (ml/s)
$\dot{q}_{pv}$ Flow through pulmonary valve (ml/s)
$\dot{q}_{pwa}$ Flow through pulmonary arterial wedge (ml/s)
$\dot{q}_{pwc}$ Flow through pulmonary capillary wedge (ml/s)
$\dot{q}_{pwv}$ Flow through pulmonary venous wedge (ml/s)
$\dot{q}_{tv}$ Flow through tricuspid valve (ml/s)
$\dot{q}_{vc}$ Flow through venae cavae (ml/s)
$\dot{Q}_v$ Venous flow source (ml/s)
R_a Peripheral arterial resistance (mmHg·s·ml^{-1})
R_{aa} Resistance of ascending aorta (mmHg·s·ml^{-1})
R_{av} Resistance of aortic valve (mmHg·s·ml^{-1})
R_{ca} Resistance of carotid artery (mmHg·s·ml^{-1})
R_{da} Resistance of descending aorta (mmHg·s·ml^{-1})
R_{mv} Resistance of mitral valve (mmHg·s·ml^{-1})
R_{pua} Pulmonary arterial resistance (mmHg·s·ml^{-1})
R_{puc} Pulmonary capillary resistance (mmHg·s·ml^{-1})
R_{puv} Pulmonary venous resistance (mmHg·s·ml^{-1})
R_{pwa} Pulmonary arterial wedge resistance (mmHg·s·ml^{-1})
R_{pwc} Pulmonary capillary wedge resistance (mmHg·s·ml^{-1})
R_{pwv} Pulmonary venous wedge resistance (mmHg·s·ml^{-1})
R_v Systemic venous resistance (mmHg·s·ml^{-1})
R_{vc} Vena caval resistance (mmHg·s·ml^{-1})
t_{ee} Time of end-ejection at maximum e_{lv} (s)
T_r Time period of cardiac cycle (s)
v_a Peripheral arterial blood volume (ml)
v_{aa} Ascending aortic blood volume (ml)
v_{da} Descending aortic blood volume (ml)
v_{heart} Total cardiac blood volume (ml)
v_{la} Chamber volume of left atrium (ml)
v_{lv} Chamber volume of left ventricle (ml)
v_{pc} Total volume of pericardial and cardiac chambers (ml)
v_{pua} Pulmonary arterial blood volume (ml)
v_{puc} Pulmonary capillary blood volume (ml)
v_{pul} Total pulmonary blood volume (ml)
v_{puv} Pulmonary venous blood volume (ml)
v_{pwa} Pulmonary arterial wedge blood volume (ml)
v_{pwc} Pulmonary capillary wedge blood volume (ml)
v_{pwv} Pulmonary venous wedge blood volume (ml)
v_{ra} Chamber volume of right atrium (ml)
v_{rv} Chamber volume of right ventricle (ml)
v_v Volume of systemic veins (ml)
v_{vc} Volume of venae cavae (ml)
V_{pc0} Pericardial volume offset (ml)
V_{pe} Pericardial fluid volume (ml)
Φ_a Peripheral arterial volume constant (ml)
Φ_{aa} Ascending aortic volume constant (ml)
Φ_{da} Descending aortic volume constant (ml)
Φ_{pc} Pericardial volume constant (ml)
Φ_{pua} Pulmonary arterial volume constant (ml)
Φ_{puc} Pulmonary capillary volume constant (ml)
Φ_{puv} Pulmonary venous volume constant (ml)
Φ_{pwa} Pulmonary arterial wedge volume constant (ml)
Φ_{pwc} Pulmonary capillary wedge volume constant (ml)
Φ_{pwv} Pulmonary venous wedge volume constant (ml)
Φ_v Systemic venous volume constant (ml)
τ_{lvc} Time constant for left ventricular contraction (s)
τ_{lvr} Time constant for left ventricular relaxation (s)
Ω Viscoelastance (mmHg·s·ml^{-1})
Ω_a Arterial viscoelastance (mmHg·s·ml^{-1})
Ω_{aa} Ascending aortic viscoelastance (mmHg·s·ml^{-1})
Ω_{ca} Carotid arterial viscoelastance (mmHg·s·ml^{-1})
Ω_{da} Descending aortic viscoelastance (mmHg·s·ml^{-1})
Ω_{la} Left atrial viscoelastance (mmHg·s·ml^{-1})
Ω_{lv} Left ventricular viscoelastance (mmHg·s·ml^{-1})
Ω_{pua} Pulmonary arterial viscoelastance (mmHg·s·ml^{-1})
Ω_{puc} Pulmonary capillary viscoelastance (mmHg·s·ml^{-1})
Ω_{puv} Pulmonary venous viscoelastance (mmHg·s·ml^{-1})
Ω_{pwa} Pulmonary arterial wedge viscoelastance (mmHg·s·ml^{-1})
Ω_{pwc} Pulmonary capillary wedge viscoelastance (mmHg·s·ml^{-1})
Ω_{pwv} Pulmonary venous wedge viscoelastance (mmHg·s·ml^{-1})
Ω_{ra} Right artial viscoelastance (mmHg·s·ml^{-1})
Ω_{rv} Right ventricular viscoelastance (mmHg·s·ml^{-1})
Ω_{vc} Vena caval viscoelastance (mmHg·s·ml^{-1})

METHODS

Five subsystems are integrated into the proposed circulatory model: electrical analog of hemodynamics, pressure coupling through the interventricular septum, volume coupling inside the pericardium, intrathoracic pressure, and baroreflex control of heart rate. Each of the five subsystems is based on previous work done by us or by other research groups extended and reconfigured to fit a unified state-space platform for numerical integration. Modeling assumptions and parameter identification are described for each subsystem as follows.

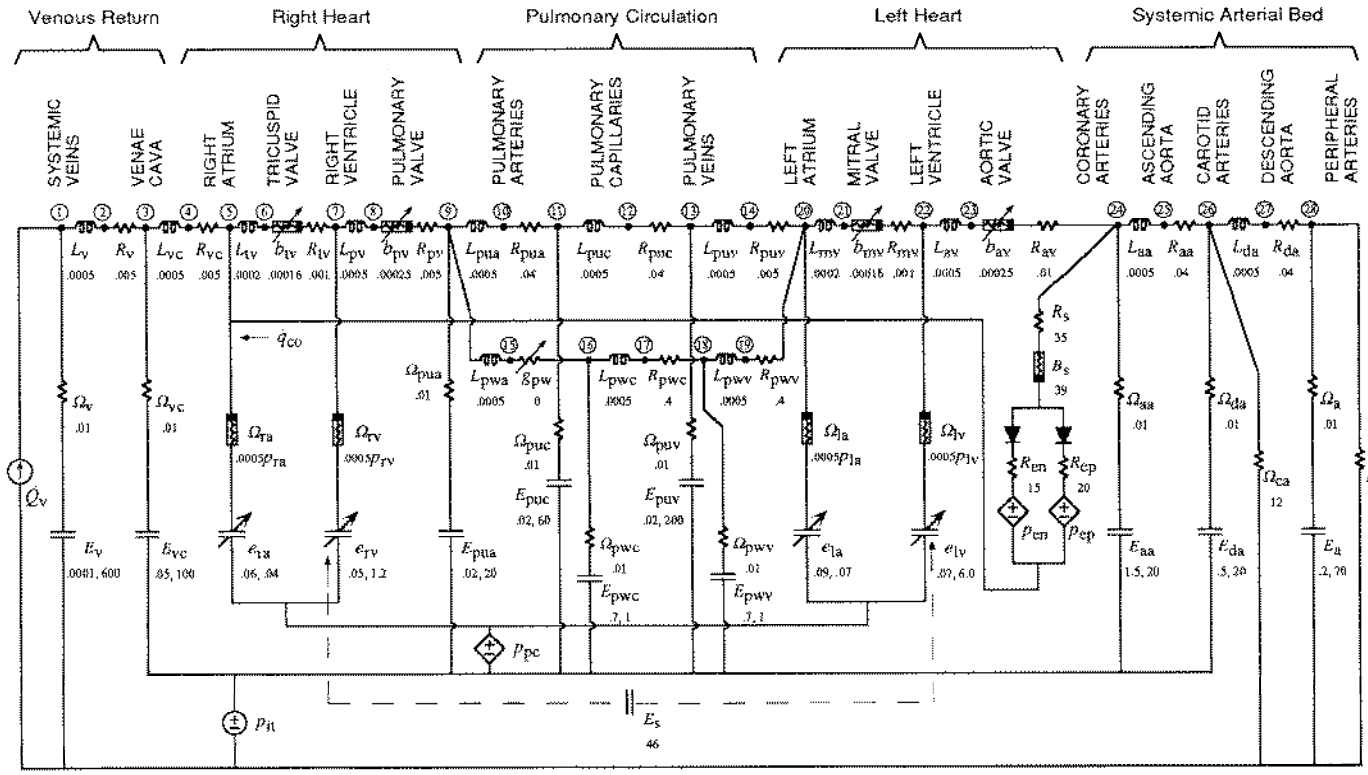

Fig. 1. Electrical analog of cardiopulmonary system. Anatomic representation is shown directly above each section of model. Model contains 74 elements: time-invariant elements are labeled by upper-case letters and time-varying elements by lower-case letters. Model elements include following types: linear resistance (R, mmHg·s·ml^{-1}), Bernoulli's resistance (B, mmHg·s^2·ml^{-2}), inertance (L, mmHg·s^2·ml^{-1}), nonlinear elastance (E) defined by E_0 (mmHg/ml) and Φ (ml), and time-varying elastance (e) defined by baseline and amplitude component (mmHg/ml). Parameter value for control is shown beneath each element label. See *Glossary* for definition of abbreviations.

Electrical analog. The right-left heart interaction through the pulmonary circulation is characterized by use of a lumped-parameter electrical analog. As shown in Fig. 1, the electrical analog is based on our previous modeling work (31, 32, 34) with the following three extensions: *1*) The original model, which represents only the left heart and a portion of the systemic arterial bed, is now extended by adding the right heart, pulmonary circulation, and systemic veins; the number of model elements increases from 33 to 74. *2*) Because the proposed model represents not only arteries but also veins and capillaries operating at a low pressure range, nonlinearity of the vascular capacitances (26) is considered. *3*) To represent the flow-dependent elements in the cardiac chambers more accurately, the internal resistances of the four contracting chambers are considered nonlinear.

In Fig. 1, time-invariant parameters are labeled by upper-case letters and time-varying parameters by lower-case letters. The basic circuit elements include the following types: Linear resistance (R) relates flow ($\dot{q}$) to pressure gradient (Δp) according to $\Delta p = R\dot{q}$. Linear inertance (L) relates time derivative of flow to pressure gradient. Bernoulli's term for a valve (B), relating squared flow to pressure gradient, is determined by the valve area (A) according to $B = \rho A^{-2}/2{,}666$ mmHg·s^2·ml^{-2}, where ρ is the density of blood (34). Vascular capacitance is assumed to be nonlinear and to have an exponential pressure-volume relationship. Different forms for the exponential pressure-volume relationship have been used in the past (14). We chose the following form, which is simple but sufficient to fit the elastance curves reported by Dahn et al. (7)

$$p = P_0 e^{v/\Phi} \qquad (1)$$

where P_0 (in mmHg) is the intercept with the transmural pressure axis and Φ (in ml) is the volume constant. Elastance (E), the reciprocal of capacitance, is defined by

$$E = \frac{dp}{dv} = \frac{P_0}{\Phi} e^{v/\Phi} = E_0 e^{v/\Phi} \qquad (2)$$

where $E_0 = P_0/\Phi$ is the zero-volume elastance (mmHg/ml). By substituting *Eq. 2* into *Eq. 1*, the transmural pressure gradient across elastance is given by $p = E\Phi$. Viscoelastance (Ω), which relates volume change in the elastic compartment to energy lost, is characterized by a linear resistance in series with the elastance in the case of a vascular compartment. In the case of a contracting chamber, Ω is represented as a nonlinear resistance that is directly proportional to the chamber pressure on the basis of the work by Shroff et al. (27).

The right atrium (RA), right ventricle (RV), left atrium (LA), and left ventricle (LV) are each modeled as a time-varying elastance (30). A time-varying elastance varies over the cardiac cycle according to an exponential charge-discharge waveform and is characterized by a baseline and an amplitude component. For example, the LV elastance is given by

$$e_{lv} = \begin{cases} E_{lva}(1 - e^{-t/\tau_{lvc}}) + E_{lvb} & 0 \le t \le t_{ee} \\ (e_{lv}|_{t_{ee}} - E_{lvb})\, e^{-(t - t_{ee})/\tau_{lvr}} + E_{lvb} & t_{ee} \le t \le T_r \end{cases} \qquad (3)$$

where $e_{lv}|t_{ee}$ is the LV elastance evaluated at end ejection. The elastance waveforms for other cardiac chambers are defined in a similar fashion. A volume dependency is applied to the ventricular elastances so that nonlinearity of the Starling

curves and load dependency of myocardial contraction can be represented. This is accomplished by scaling the ventricular elastance by a factor derived from the end-diastolic ventricular volume, as described previously (34).

In Fig. 1 the pulmonary circulation begins at the pulmonary valve (*node 9*) and ends at the left atrium (*node 20*). The circuit segment from *node 15* to *node 19* is a special provision for the pulmonary capillary wedge pressure (p_{pw}). By setting conductance (g_{pw}) = 0, flow ceases in this segment and p_{pw} measured at *node 16* should reflect the LA pressure.

Interventricular septum. Direct pressure coupling between the RV and LV through the interventricular septum is characterized by use of the model developed by Maughan et al. (20). Their model consists of three elastic compartments. In addition to the RV and LV freewall compartments (e_{rv} and e_{lv}), shift of the septum is also represented by an elastic compartment (E_s). Under this assumption, the LV pressure is the sum of the effective LV elastance times volume and the "cross-talk" pressure from the RV

$$p_{lv} = \hat{e}_{lv} v_{lv} + k_{rl} p_{rv} \tag{4}$$

where $k_{rl} = e_{lv}/(E_s + e_{lv})$ and $\hat{e}_{lv} = E_s k_{rl}$. Similarly, the RV pressure is given by

$$p_{rv} = \hat{e}_{rv} v_{rv} + k_{lr} p_{lv} \tag{5}$$

where $k_{lr} = e_{rv}/(E_s + e_{rv})$ and $\hat{e}_{rv} = E_s k_{lr}$. Because the cross-talk gains (k_{rl} and k_{lr}) can be computed from the three elastances (i.e., e_{rv}, e_{lv}, and E_s), the transseptal pressure coupling can be represented completely by E_s. Maughan et al. measured E_s in isolated canine hearts that were free from the pericardial influence and had about the same ventricular elastances as those in our model. Thus it should be suitable to adopt their experimental data directly to our model; the value of 45.9 mmHg/ml is assigned to E_s.

Pericardium. In addition to transseptal pressure coupling, volume coupling exists among all chambers in the pericardium. In our model, pericardial dynamics are represented by a pericardial compartment with an exponential pressure-volume relationship. The pericardial pressure (p_{pc}) is controlled by the total chamber volume in the pericardium according to the exponential relationship. This pressure exerts on all cardiac chambers through the free walls of atria and ventricles. The total fluid volume in the pericardium (v_{pc}) is the sum of the volume of the heart chambers (v_{heart}) and the pericardial fluid volume (V_{pe})

$$v_{pc} = v_{heart} + V_{pe} \tag{6}$$

v_{heart} is given by

$$v_{heart} = v_{ra} + v_{rv} + v_{la} + v_{lv} \tag{7}$$

This formula is similar to but slightly different from that employed by Beyar et al. (1). Our formula includes V_{pe} and excludes the myocardial volume, because the change in myocardial volume relative to the total heart volume is negligibly small. The pressure-volume relationship in the pericardium is an exponential function (1, 2)

$$p_{pc} = K_{pc} e^{(v_{pc} - V_{pc0})/\Phi_{pc}} \tag{8}$$

The volume offset (V_{pc0}) is set at 380 ml, the volume constant (Φ_{pc}) is set at 40 ml, and K_{pc} is set at 1. These parameter values are determined on the basis of the pericardial pressure-volume relationships reported by Freeman and LeWinter (10).

Intrathoracic pressure. The respiratory effect on hemodynamics is represented as a time-varying intrathoracic pressure. A respiratory cycle has a period of 5 s, comprising 2 s of inspiration and 3 s of expiration. On the basis of data reported by Guyton (12), intrathoracic pressure (p_{it}) is assumed to vary over time according to an exponential charge-discharge waveform with a baseline (P_{itb}) of −3.7 mmHg and an amplitude (P_{ita}) of −1.8 mmHg. In other words, p_{it} varies from −3.7 mmHg during expiration to −5.5 mmHg during inspiration. The intrathoracic pressure is incorporated into the electrical analog by applying p_{it} directly to all compartments in the thorax, which include venae cavae, right heart, pulmonary circulation, left heart, and aorta.

Baroreflex control of heart rate. Sinoaortic baroreflex control of heart rate is approximated by a first-order relationship between the cardiac period and the systolic aortic pressure. As arterial pressure decreases, heart rate is increased by the sinoaortic baroreflex (6). The relationship between heart rate and arterial pressure is generally nonlinear. However, within the normal range of arterial pressure variation, a linear approximation to the relationship between heart rate and arterial pressure should be acceptable. Further support for the validity of this assumption comes from the product of heart rate and systolic arterial peak pressure. This product has been used as an index for myocardial oxygen consumption (23), which is based on the implicit assumption of an inverse relationship between heart rate and systolic arterial peak pressure for a given level of myocardial oxygen consumption. In the present model the following first-order relationship between the cardiac period (T_r) and the systolic aortic pressure is used to characterize the baroreflex control of heart rate

$$T_r = G_{baro} (\text{systolic } p_{ao} - 120) + 0.855 \text{ (s)} \tag{9}$$

where the baroreflex gain (G_{baro}) is set at 0.005 s/mmHg. The coefficients in the above equation are determined by assuming the following two reference points: heart rate is 70 beats/min at systolic aortic pressure (p_{ao}) = 120 mmHg and increases to 85 beats/min at systolic p_{ao} = 90 mmHg.

State-space representation and numerical solution. The electrical analog is an effective means for constructing the model, integrating various mechanisms into circulatory dynamics, and relating model parameters to their physical meanings. The analog model is also used to derive the mathematical model in the form of a state-space representation that characterizes the instantaneous dynamics for the entire system. For the present model the state-space representation comprises 28 differential equations obtained by a nodal analysis of the analog circuit. State variables include the volume of every elastance and the flow through every inertance. The state (differential) equation for each state variable is derived on the basis of continuity of flows at the appropriate node in the circuit. The 28 nodes corresponding to the 28 state equations are marked by circled numbers in Fig. 1. The 28 state equations and the nodal analysis technique are given in the APPENDIX. The state equations are numerically integrated by use of a second-order Runge-Kutta method at a time step of 1 ms. The nonlinear elements, including elastances and valves, are updated at a time step of 5 ms. This choice of the order and parameters for the numerical method has provided numerical stability and an appropriate compromise between round-off error and truncation error on the basis of our previous experiences with similar models. The model-based simulation software was written completely in the C language and runs on any Macintosh-type computer (Apple Computer, Cupertino, CA).

Parameter identification. Identification of the parameters in the electrical analog is accomplished in two steps. In the first step, the model parameters are grossly estimated in terms of the physiological range or the order of magnitude for the parameter value. The vascular resistances and inertances are calculated on the basis of fluid dynamic laws and the dimensions of the anatomic compartments that the individual sections of the model represent (31). The valve parameters (an inertance, a linear resistance, and a Bernoulli term for each valve) are determined on the basis of a previous study using Doppler echocardiographic data (34). In the second step, the model parameters are fine tuned in the dynamic situations with the simulation running continuously. The model parameters are iteratively adjusted within their physiological ranges while the resulting pressure and flow waveforms in the entire system are monitored. A major determinant of the circulatory dynamics is the vascular elastance, which is nonlinear and specified by two parameters (E_0 and Φ). The volume at each section of the lumped-parameter circuit is mainly controlled by the elastance. Table 1 summarizes the volumes in different parts of the circulatory system reported by Engelberg and DuBois (9) and Guyton (12). The volume distribution provides crucial information for determining the elastances. For each elastance, E_0 and Φ are iteratively adjusted until a reasonable representation for the hemodynamic waveforms and the average volume stored in the elastance is achieved. The volume constant Φ is generally on the same order of magnitude as the volume in the elastance, which is a useful rule of thumb for identifying Φ. The resulting volume distribution represented by the model is also shown in Table 1. The baseline elastances for the contracting chambers are also determined on the basis of volume distribution in the heart. The viscoelastic terms are on the order of 10^{-2} mmHg·s·ml^{-1} on the basis of the degree of damping of the pressure waveforms. The proportionality constant for the pressure-dependent internal chamber resistance is set at 5×10^{-3} s/ml, which is three times smaller than that determined by Shroff et al. (27) in cannulated canine ventricles. A smaller value is more appropriate here, because the valve device in our model accounts for a significant portion of the flow-dependent components at the outflow tract of a contracting chamber. This proportionality constant is applied to all four cardiac chambers. The values of all model parameters that have been identified to define the baseline hemodynamics in this study are given in Fig. 1.

Sensitivity analysis of model parameters. A sensitivity analysis is conducted to determine how the simulated hemodynamics are affected by each model parameter individually. The sensitivity is quantified by computing a gain factor according to

$$\text{sensitivity gain} = \frac{\%\ \text{change of affected (hemodynamic) index}}{\%\ \text{change of affecting (model) parameter}} \quad (10)$$

The hemodynamic indexes include heart rate; cardiac output; systolic/diastolic p_{ao}; end-diastolic RV (p_{rv}), LV (p_{lv}), and pulmonary arterial pressures (p_{pa}) and RV (v_{rv}) and LV volumes (v_{lv}); and mean RA (p_{ra}) and LA pressures (p_{la}) and total pulmonary (v_{pul}), total cardiac (v_{heart}), and systemic venous blood volumes (v_v). These 14 parameters are chosen because they are routinely measured in clinics or they are major determinants of the physiological state of the cardiovascular system. The model parameters include all parameters shown in Fig. 1 and the variables in *Eqs. 8* and *9*. Eighty-five model parameters are included in the sensitivity study. In each case, the model parameter is perturbed by a 10% increase from its control value. Before the hemodynamic indexes are recorded, the simulation is allowed to run for several cardiac cycles until the initial transients subside. The individual contribution of pericardial and transseptal coupling to hemodynamics is also studied by removing pericardial compression ($K_{pe} = 0$) or septal elastance ($E_s \to \infty$). In the latter case, a large value is assigned to E_s in the actual simulation.

Venous return. The flow source ($\dot{Q}_v$) returns a constant flow into the venous reservoir represented by E_v. Buffered by the large volume of the venous reservoir, $\dot{Q}_v$ exerts its effect on the cardiac output over a relatively long period of time. Instead of $\dot{Q}_v$, $\dot{q}_v$, which is the flow through venous inertance (L_v), should be considered as the venous return in this model on the cycle-by-cycle basis. Because at steady state $\dot{Q}_v$ must be equal to mean $\dot{q}_v$ and cardiac output, $\dot{Q}_v$ does provide an extra degree of freedom for controlling the preload. However, this degree of freedom is mainly related to the setting of the venous pressure and has only a minor effect on the cardiac output, as demonstrated later. The procedure for setting $\dot{Q}_v$ in the simulations of the disease conditions is as follows. After the change in a circulatory parameter, $\dot{Q}_v$ is initially maintained at control, i.e., 83.3 ml/s or 5 l/min. The initial transients caused by the parameter change usually subside within the first 10 cardiac cycles. Then the difference between $\dot{Q}_v$ and mean $\dot{q}_v$ causes a charge or a discharge of the venous reservoir. Accordingly, the venous pressure increases or decreases and drives the cardiac output closer to $\dot{Q}_v$. The change in cardiac output occurs very gradually. To define the operating point for $\dot{Q}_v$ in a consistent way, we allow the simulation to run for 50 cardiac cycles after the change in a model parameter. At this point $\dot{Q}_v$ is set equal to the cardiac output to ensure a steady state.

Model-based study of cardiovascular physiology. The model-based study consists of two parts. First, the model parameters are adjusted to fit clinical data. The clinical data include the pressure measurements in the right and left heart from a patient who has undergone cardiac catheterization and the pulsed-Doppler echocardiographic recordings of transmitral and pulmonary venous flow velocities from a previous study (34). These data were originally recorded in hard-copy forms and scanned into a digital computer for comparison with the model-generated waveforms. Second, the model is used to predict the hemodynamic consequences by adjusting model parameters that correspond to the causes of various disease conditions. The following conditions are studied: mitral valve stenosis (MS), mitral regurgitation, LHF, right heart failure

Table 1. *Model representation of blood volume distribution in human circulatory system*

	Blood Volume Distribution		Model Representation	
	%*	Volume,† ml	Variables	Volume, ml
Heart	7	350	v_{heart}	351
Pulmonary circulation	9	450	v_{pul}	438
Pulmonary arteries	2.3	115	v_{pua}	75
Pulmonary capillaries	1.3	65	v_{puc}	150
Pulmonary veins	5.4	270	v_{puv}	213
Systemic arteries	13	650	$v_{aa} + v_{da} + v_a$	186
Systemic capillaries	7	350	None	0
Systemic veins	64	3,200	$v_v + v_{vc}$	2,628

See *Glossary* for definition of abbreviations. *Based on data reported by Engelberg and DuBois (9) and Guyton (12). †Based on assumption that total blood volume is 5,000 ml.

(RHF), cardiac tamponade, pulsus paradoxus, and the Valsalva maneuver. These simulations are intended for acute situations without the chronic adaptation effects, such as enlargement and hypertrophy of atria and ventricles.

RESULTS

Baseline hemodynamics. Figure 2 shows the pressures, flows, and volumes in the right and left heart for normal physiology. These waveforms are generated by the model with parameter values given in Fig. 1. The wave shapes are generally in accord with in vivo data. Specifically, atrial pressures (p_{ra} and p_{la}) show the characteristic shapes of the a wave, c wave, x descent, v wave, and y descent. For transtricuspid flow ($\dot{q}_{tv}$) and transmitral flow ($\dot{q}_{mv}$), the E and A waves are accurately represented. For venous return flow ($\dot{q}_{vc}$) and pulmonary venous flow ($\dot{q}_{mv}$), the bimodal wave shape (S and D) and the end-diastolic flow reverse are consistent with in vivo observations (5). The wave shapes for flows through the pulmonary valve ($\dot{q}_{pv}$) and the aortic valve ($\dot{q}_{av}$) are also accurate. Table 2 shows the hemodynamic indexes computed from the model-generated waveforms. This simulation defines the baseline hemodynamics and is used as control in the subsequent studies.

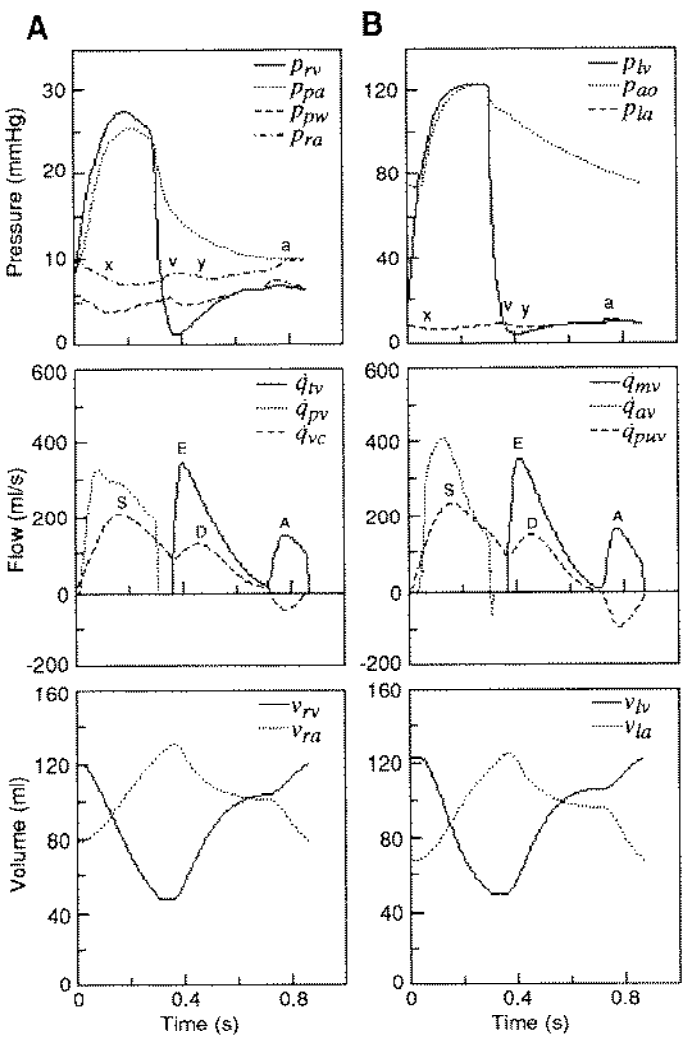

Fig. 2. Simulated baseline hemodynamics for right heart (*A*) and left heart (*B*). See *Glossary* for definition of abbreviations.

Sensitivity analysis. The simulated hemodynamics are insensitive to most individual model parameters. The result of the sensitivity analysis is summarized in Table 3, in which only those model parameters with at least one gain ≥0.1 are listed. Model parameters with all gains <0.1 are considered insensitive and are excluded from Table 3 in an effort to reduce the large amount of data. Inertance (L), R, and Ω values in the model are generally insensitive, with all gains <0.1. The only exception is systemic afterload resistance (R_a), which is a major determinant of cardiac output and aortic pressure. The vascular capacitances are also insensitive with the exception of preload capacitances for right heart (E_v, Φ_v) and left heart (E_{puv}, Φ_{puv}). Contractility of the heart is defined by the elastance baselines and amplitudes of the atria and ventricles; these parameters are relatively sensitive. Pericardial volume offset (V_{pe0}) and intrathoracic pressure baseline (P_{itb}) are sensitive, whereas G_{baro} and E_s are not.

Model fit to clinical data. Figure 3*A* shows six pressure waveforms obtained from the catheterization record for a 60-yr-old female patient with severe mitral regurgitation and congestive heart failure. The model parameters are adjusted to provide a simultaneous fit to all six waveforms (Fig. 3*B*). Figure 4 shows the pulsed-Doppler echocardiographic recordings of transmitral and pulmonary venous flow-velocity waveforms obtained from a previous study (34). *Patients A, B,* and *C* represent normal LV function, significant LV dysfunction (functional class II–III), and severe LV dysfunction (functional class IV), respectively. Superimposed on the pulsed-Doppler recordings are the corresponding waveforms generated by the present model. The waveforms from the previous left heart model are also included to provide a reference for the absence of the right heart dynamics. Compared with the previous model, the present model provides a slightly improved fit, especially to the pulmonary venous flow-velocity waveforms.

Venous return. Figure 5*A* shows the cardiac output over 100 cardiac cycles after the parameter change for each disease condition. To evaluate the choice for the operating points of venous return, $\dot{Q}_v$ was maintained at control, i.e., 5 l/min, over these 100 cycles. The vertical bars mark the points after 50 cardiac cycles where the disease conditions are defined. In Fig. 5*B* these operating points are also shown on the cardiac output vs. mean p_{ra} curves.

Mitral valve abnormalities. Mitral valve abnormalities are simulated by changing the mitral valve area (A_{mv}) in the model. For control, A_{mv} = 4 cm^2 when the mitral valve opens and zero when the mitral valve closes. In clinical situations, MS is considered mild for open A_{mv} = 2 cm^2 and severe for open A_{mv} = 1 cm^2 (4). In this study a severe case of MS is simulated by reducing open A_{mv} from 4 to 1 cm^2. As shown in Fig. 6*A*, the model predicts the typical hemodynamic consequences of MS, i.e., the increase in diastolic LA-LV pressure gradient and transmitral E-wave flow deceleration time. Data in

Table 2. *Hemodynamic indexes for control and percent changes relative to control for MS, MR, RHF, LHF, and cardiac tamponade*

	Heart Rate	Cardiac Output	Systolic p_{ao}	Diastolic p_{ao}	End-Diastolic p_{rv}	End-Diastolic p_{lv}	End-Diastolic p_{pa}	End-Diastolic v_{rv}	End-Diastolic v_{lv}	Mean p_{ra}	Mean p_{la}	Mean v_{pul}	Mean v_{heart}	Mean v_v
							Control							
	70 beats/min	5.0 l/min	122 mmHg	75 mmHg	6.3 mmHg	9.3 mmHg	9.8 mmHg	120 ml	123 ml	5.3 mmHg	8.1 mmHg	452 mmHg	375 ml	2,765 ml
							%Change relative to control							
MS	8	−6	−9	−4	15	−5	60	1	−15	30	74	23	7	5
MR	26	−34	−28	−28	178	162	170	−9	21	213	222	52	19	22
LHF mild	8	−12	−10	−7	48	57	54	−5	19	67	68	21	11	9
LHF severe	26	−26	−27	−19	131	139	131	−16	38	174	162	42	19	19
RHF mild	7	−7	−10	−4	42	−8	−2	25	−14	50	−4	−2	6	8
RHF severe	19	−17	−22	−11	97	−6	4	53	−32	116	2	0	11	15
Tamponade	45	−36	−41	−27	251	137	131	−46	−60	300	162	41	−47	27

MS, mitral stenosis; RHF and LHF, right and left heart failure; MR, mitral regurgitation. See *Glossary* for definition of other abbreviations.

Table 2 show that the effect of MS propagates backward to the right heart, increasing end-diastolic p_{pa} by 60% and mean p_{ra} by 30%.

MR is simulated by increasing the closed A_{mv} from 0 to 1 cm^2. As shown in Fig. 6*B*, the model predicts the large v wave in p_{la} typically associated with MR. Data in Table 2 show that end-diastolic p_{lv} increases by 162% and end-diastolic v_{lv} increases by 21%. The decrease in systemic arterial pressure causes a baroreflex increase in heart rate from 70 beats/min (control) to 88 beats/min (26%). Cardiac output decreases by 34%. The effect of MR is extended to the pulmonary circulation and the right heart. Damming of blood in the pulmonary system is evidenced by the increase in mean v_{pul} by 52%. Mean right atrial pressure rises from 5.3 mmHg (control) to 17 mmHg (213%). The venous blood volume also increases by 22%.

LHF. LHF is simulated by decreasing LV contractility. In the simulation, LV elastance amplitude (E_{lva}) is reduced from 6.0 to 3.0 mmHg/ml (50% reduction) in a mild case of LHF and to 1.5 mmHg/ml (75% reduction) in a severe case of LHF. Figure 7*A* shows the hemodynamic waveforms resulting from severe LHF. Mean p_{la} rises from 8.1 to 21 mmHg (162%), and end-diastolic p_{lv} rises from 9.3 to 22 mmHg (139%). Heart rate increases from 70 to 88 beats/min. The effect of LHF propagates backward to the right heart and causes an increase in mean p_{ra} from 5.3 to 15 mmHg (174%). Mean v_{pul} increases from 452 to 642 ml (42%). Mean v_v increases from 2,765 to 3,290 ml (19%). Cardiac output decreases from 5.0 to 3.7 l/min (−26%). The left heart is enlarged, whereas the right heart is suppressed, as evidenced by the volume waveforms in Fig. 7*A*. For mild LHF the hemodynamic consequences are much less serious. End-diastolic p_{lv} rises moderately from 9.3 to 15 mmHg (57%) and mean p_{ra} from 5.3 to 8.9 mmHg (67%).

RHF. RHF is simulated by decreasing RV contractility. In the simulation, RV elastance amplitude (E_{rva}) is reduced from 1.2 to 0.6 mmHg/ml (50% reduction) in a mild case of RHF and to 0.3 mmHg/ml (75% reduction) in a severe case of RHF. Figure 7*B* shows the hemodynamic waveforms resulting from severe RHF. The right heart can no longer sustain normal cardiac output (−17%). However, the hemodynamic consequence is

Table 3. *Sensitivity analysis in terms of gain computed as percent change of affected index (columns) divided by percent change of affecting parameter (rows)*

	Heart Rate	Cardiac Output	Systolic p_{ao}	Diastolic p_{ao}	End-Diastolic p_{rv}	End-Diastolic p_{lv}	End-Diastolic p_{pa}	End-Diastolic v_{rv}	End-Diastolic v_{lv}	Mean p_{ra}	Mean p_{la}	Mean v_{pul}	Mean v_{heart}	Mean v_v
R_a	−0.3	−0.6	0.3	0.4	0.2	0.3	0.1	−0.2	−0.1	0.3	0.3	0.1	0.1	0.1
E_{v0}	−0.1	0	0	0	0.6	0.3	0.4	0.1	0	0.8	0.4	0.2	0.1	−0.1
Φ_v	0	−0.1	−0.2	−0.1	−1.8	−0.8	−0.9	−0.6	−0.1	−2.3	−1.0	−0.4	−0.4	0.2
E_{puv0}	−0.1	0.1	0.1	0	0.2	0.2	0.2	0	0	0.2	0.2	−0.3	0	0
Φ_{puv}	0	0	0	0	0	0	0	0	0	0.1	0	0.1	0	0
E_{rva}	−0.1	0.1	0	0	0.1	0.1	0.1	0	0	0	0.1	0.1	0	0
E_{rvb}	−0.1	0.1	0.1	0	0	0.1	0	0	0.1	0.1	0	0	−0.1	0
E_{lva}	−0.1	0.1	0.1	0	−0.1	0.3	0.2	−0.3	0.1	−0.1	0.3	0.1	0	0
E_{lvb}	0.1	−0.1	−0.1	−0.1	0.5	−0.4	−0.3	−0.3	−0.2	0.3	−0.4	−0.2	−0.1	0.1
E_{laa}	−0.1	0.1	0.1	0	0	0.1	0	0	0	0	0	0	0	0
E_{lab}	−0.1	0.1	0.1	0	0.1	0.1	0.2	0.1	0	−0.1	0.3	0.1	−0.1	0
E_{lvd}	−0.1	0.1	0.1	0	0.1	−0.2	−0.2	0.1	−0.2	0	−0.2	−0.1	−0.1	0
E_{lvb}	0.1	−0.1	−0.2	−0.1	−0.1	0.7	0.6	−0.1	−0.3	0	0.7	0.2	0.1	0
V_{per0}	−0.2	0.2	0.2	0.1	−0.1	0.2	−0.1	0.6	0.5	−0.4	0	0.1	0.6	0
P_{stb}	0	0	0.1	0	0.2	0.2	0.2	−0.1	0	0.2	0.2	−0.1	−0.1	0

See *Glossary* for definition of abbreviations.

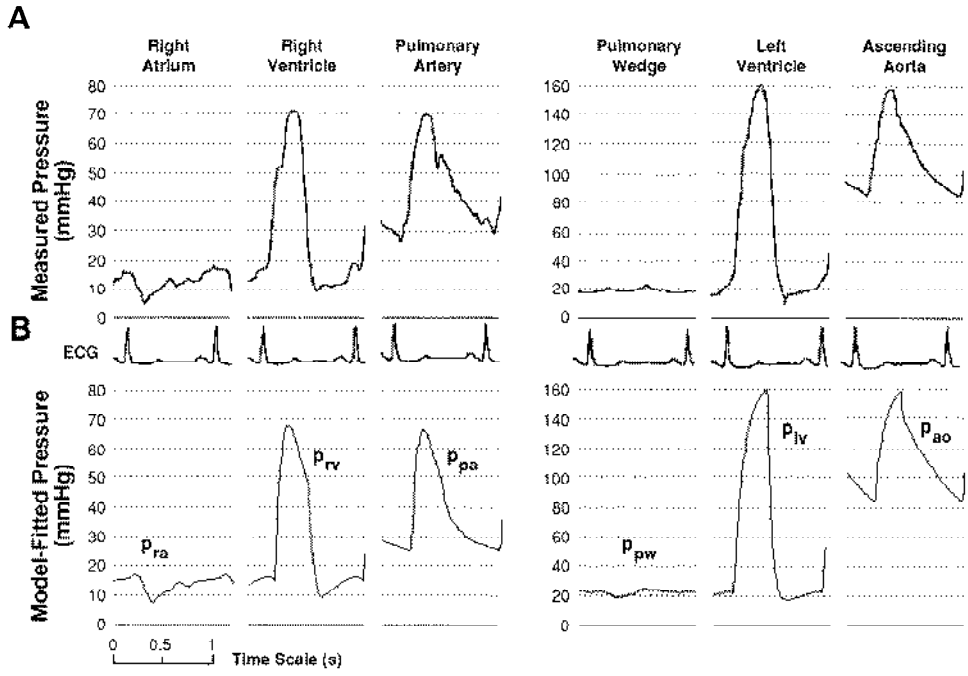

Fig. 3. Clinically measured pressure waveforms (*A*) and corresponding model-fitted waveforms (*B*). See *Glossary* for definition of abbreviations.

generally less severe than that of severe LHF. Mean p_{ra} rises from 5.3 to 11 mmHg (116%), and heart rate increases from 70 to 83 beats/min (19%). Mean v_v increases from 2,765 to 3,180 ml (15%). The right heart is enlarged, whereas the left heart is suppressed, as evidenced by the volume waveforms in Fig. 7*B*. For mild RHF, mean p_{ra} rises from 5.3 to 8.0 mmHg (50%) and cardiac output is slightly decreased from 5.0 to 4.7 l/min (−7%).

Cardiac tamponade. In clinical situations the symptoms of cardiac tamponade usually appear when V_{pe} exceeds 150 ml (5, 10). In the simulation, acute cardiac tamponade is induced by increasing V_{pe} from 30 ml in control to 300 ml. Figure 8 shows the steady-state hemodynamic waveforms after the increase in V_{pe}. Pericardial pressure (p_{pe}) increases from the normal range of 1–4 mmHg to 17–23 mmHg. The volume of all four cardiac chambers is significantly suppressed from

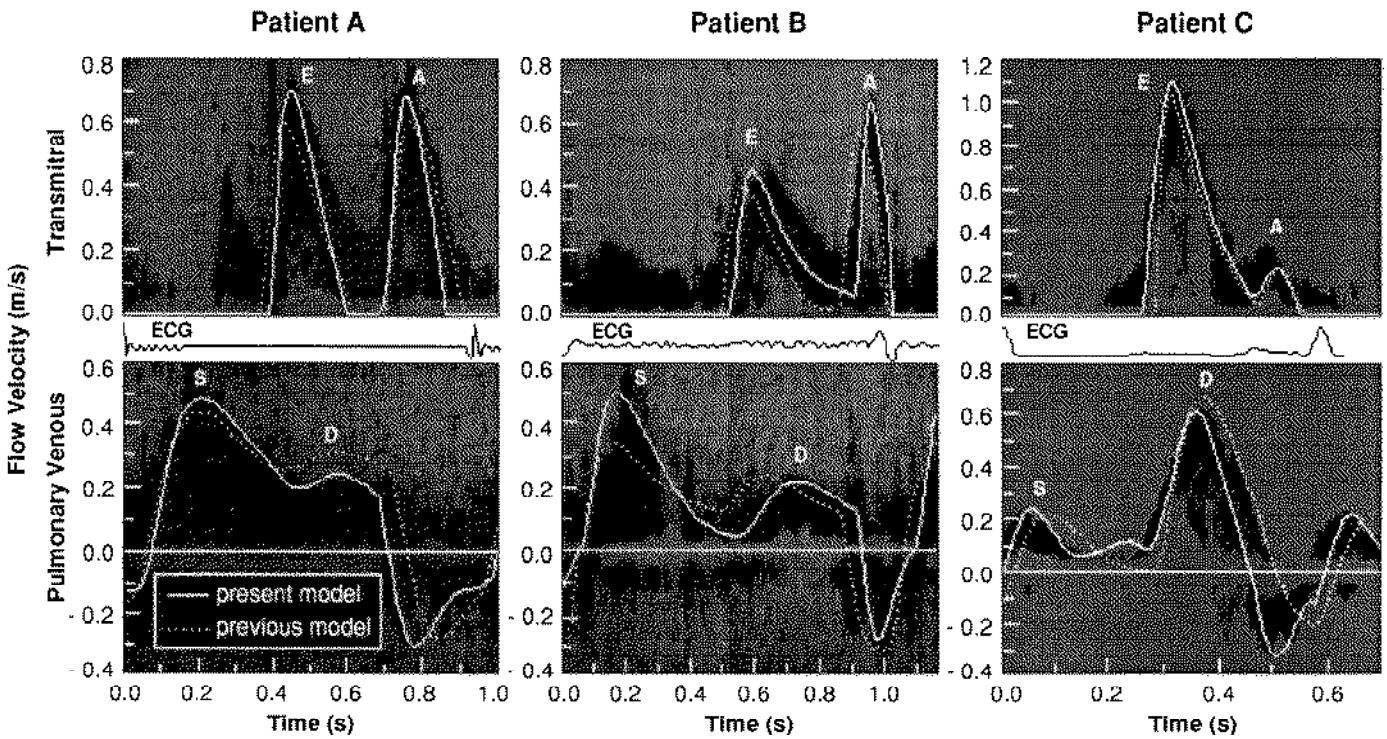

Fig. 4. Pulsed-Doppler echocardiographic recordings from 3 patients on which are superimposed waveforms fitted with present model and previous model, which does not include right heart dynamics.

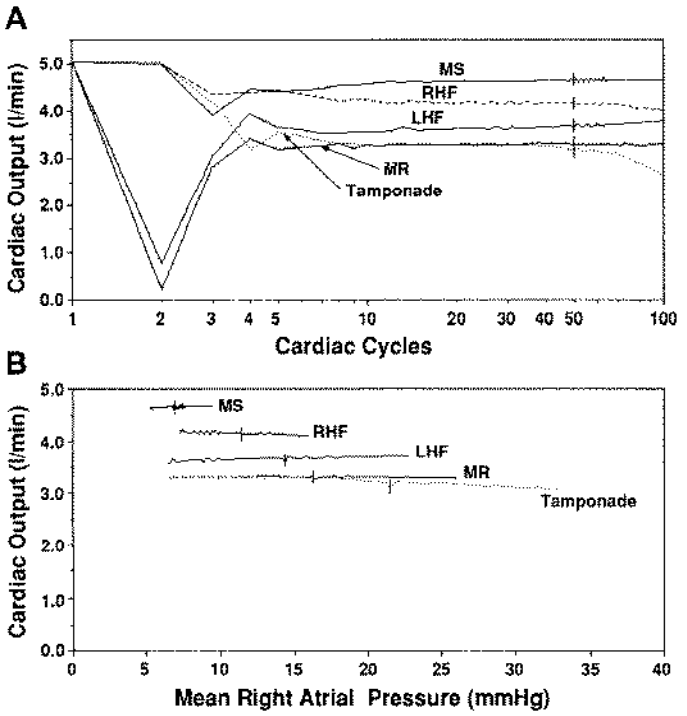

Fig. 5. Cardiac output over 100 cardiac cycles after change of model parameter with cardiac cycles shown on log scale (*A*) and cardiac output vs. mean right atrial pressure (*B*). Venous flow source was maintained at control. Vertical bars, points after 50 cardiac cycles at which various disease conditions were defined: mitral stenosis (MS), mitral regurgitation (MR), left heart failure (LHF), right heart failure (RHF), and cardiac tamponade.

a total of 375 ml (control) to 199 ml (−47%). Cardiac tamponade is evidenced by the equalization of end-diastolic p_{ra}, p_{rv}, p_{pa}, p_{la}, and p_{lv}. Mean p_{ra} rises from 5.3 to 21 mmHg (300%). Damming of blood in the pulmonary circulation and systemic veins is evidenced by the increase in mean v_{pul} from 452 to 637 ml (41%) and mean v_v from 2,765 to 3,512 ml (27%). Heart rate increases from 70 to 102 beats/min (45%). Cardiac output decreases from 5.0 to 3.2 l/min (−36%).

Pulmonary capillary wedge pressure. The waveforms of p_{pw} in the above simulations are shown in Fig. 9 for comparison. The p_{la} for control is also shown. Compared with p_{la}, p_{pw} is delayed by 100 ms and its dynamic magnitude is damped by 2 mmHg. These parameters are within the range of in vivo data (17), which show 2- to 4-mmHg damping and 100- to 150-ms delay in the p_{pw}.

Pulsus paradoxus. The condition of pulsus paradoxus is present when the inspiratory fall of systolic arterial pressure (IFSAP) exceeds 10 mmHg (25). Pulsus paradoxus is a condition often associated with cardiac tamponade. The simulation of pulsus paradoxus is accomplished by inducing cardiac tamponade (V_{pe} = 300 ml) and changing the intrathoracic pressure amplitude (P_{ita}) from −1.8 mmHg (control) to −8 mmHg. The latter is based on experimental observations in dogs (25) showing an increased intrathoracic pressure during cardiac tamponade. The respiratory effect on p_{ao} is shown in Fig. 10*A* for control (IFSAP = 5 mmHg) and in Fig. 10*B* for pulsus paradoxus (IFSAP = 13 mmHg). In the case of pulsus paradoxus, the pulse pressure (systolic-diastolic pressure difference) is 27 mmHg during expiration and falls to 19 mmHg during inspiration. The transseptal coupling has no effect on pulsus paradoxus: When the transseptal coupling is removed during pulsus paradoxus, IFSAP remains unchanged.

Valsalva maneuver. Simulation of the Valsalva maneuver is accomplished by increasing p_{it} to 40 mmHg during a prolonged expiration period of 10 s. Figure 10*C* shows the p_{ao} along with p_{it} before, during, and after the Valsalva maneuver. The four phases of the Valsalva maneuver are demonstrated by the model-generated p_{ao} waveform: *1*) A transient rise occurs at the onset of the forced expiration. *2*) Arterial pressure pulses are suppressed during the strain period, and the baroreflex causes heart rate to increase. *3*) A transient decrease occurs at the release of the intrathoracic pressure. *4*) Arterial pressure rises above the normal level and the baroreflex causes bradycardia.

Transseptal and pericardial coupling. In Fig. 11 the hemodynamic consequences of removing transseptal or pericardial coupling are shown by use of the pressure-volume loops for the four cardiac chambers. The shapes of the pressure-volume loops for control are accurately represented for ventricles (30) and atria (18). The pressure-volume loops are altered slightly by removing transseptal coupling, significantly by removing pericardial coupling, and drastically by inducing cardiac tam-

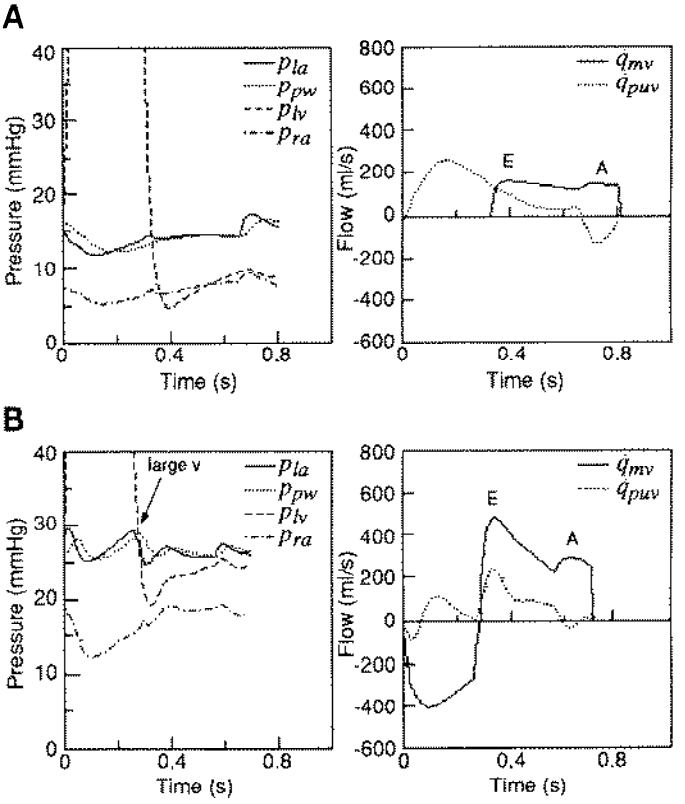

Fig. 6. Hemodynamics for mitral valve abnormalities: mitral stenosis was simulated by decreasing open mitral valve area from 4 to 1 cm^2 (*A*), and mitral regurgitation was simulated by increasing closed mitral valve area from 0 to 1 cm^2 (*B*). See *Glossary* for definition of abbreviations.

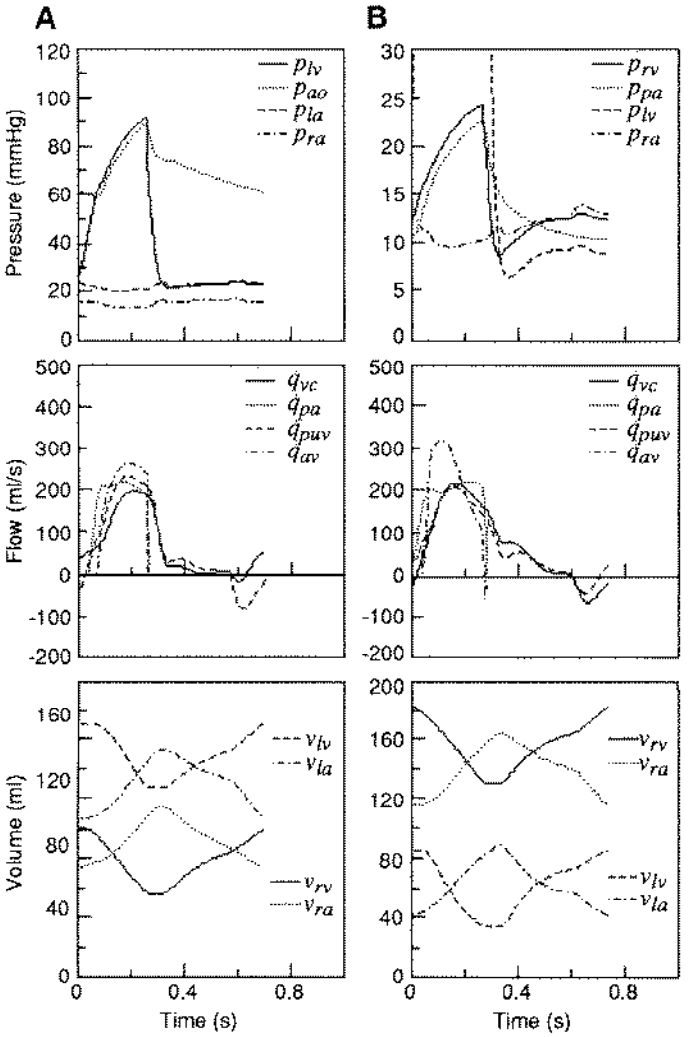

Fig. 7. Hemodynamics for left heart failure with left ventricular contractility reduced by 75% (*A*) and right heart failure with right ventricular contractility reduced by 75% (*B*). See *Glossary* for definition of abbreviations.

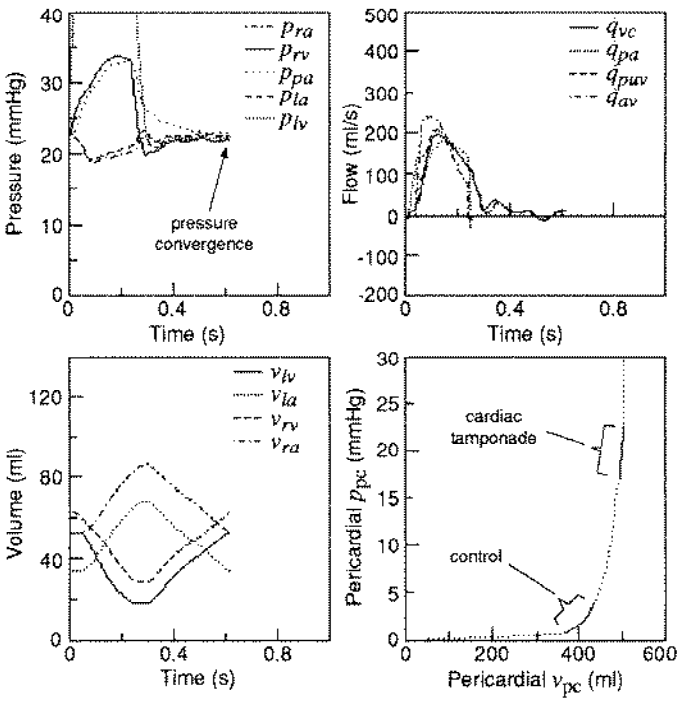

Fig. 8. Hemodynamics for cardiac tamponade induced by increasing pericardial fluid volume from 30 ml (control) to 300 ml. Operating range on pericardial pressure-volume curve is shown at *bottom right* for control and cardiac tamponade. See *Glossary* for definition of abbreviations.

ponade. In Table 4 the coupling effects on the hemodynamic indexes are shown as percent changes with respect to control. Santamore and Burkhoff (24) incorporated a higher level of transseptal coupling in their model of the canine heart by assigning E_s = 20 mmHg/ml. To compare with their data, we also reduce E_s from 45.9 to 20 mmHg/ml and include the result in Table 4.

DISCUSSION

A comprehensive model of cardiopulmonary circulation has been developed by incorporating hemodynamics, respiratory effects, pericardial dynamics, and baroreflex control into a single integrated model. Several modeling methods based on previous work have been adopted in the present study: The electrical analog is an extension of our previous models (32, 34), and the approach can be traced to the early work by Snyder et al. (29); the pericardial volume coupling is based on data reported by Freeman and LeWinter (10) and is similar to a model employed by Beyar et al. (1); the transseptal pressure coupling is based on the work by Maughan et al. (20); the exponential pressure-volume relationship for vascular capacitance is based on data reported by Dahn et al. (7); and the baroreflex model, as a first-order approximation to the relationship between heart rate and systolic arterial pressure, is derived from the result by Robinson (23).

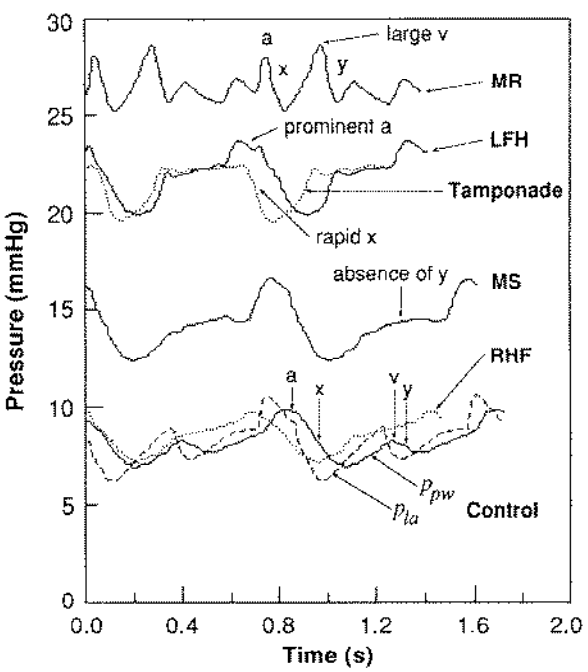

Fig. 9. Simulated p_{pw} for various physiological conditions specified in Table 2. For control, p_{la} (dashed line) is also shown. See *Glossary* for definition of abbreviations.

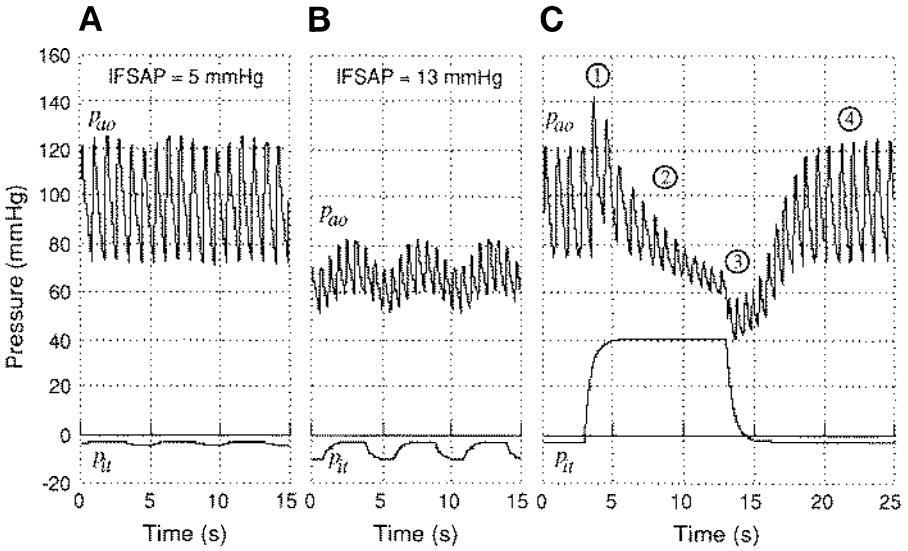

Fig. 10. Simulations of respiratory effects on aortic pressure for control (*A*), pulsus paradoxus (*B*), and Valsalva maneuver (*C*). Model demonstrates 4 phases of Valsalva maneuver: *1*) transient rise, *2*) suppressed pulses, *3*) transient decrease, and *4*) reflex bradycardia. See *Glossary* for definition of abbreviations.

The significance of the present model lies in its ability to generate a broad spectrum of hemodynamic waveforms for transient and steady-state and for normal and pathological physiology. Versatility and accuracy of the model should be attributed to the use of state-space representation as a common platform for integrating the various modeling methods. The state-space representation completely characterizes the system's dynamics with the 28 state equations. The nonlinear, time-varying, and control elements are indirectly incorporated through the coefficients of the state equations, instead of direct exertion on the state variables themselves. We carefully avoid modifying state variables directly, because such a modification is likely to create a discontinuity, resulting in numerical instability. The coefficients of the state equations are constantly updated at a time step of 5 ms, while the state variables are numerically integrated at a time step of 1 ms according to the physical principles from which the state equations are derived. It is demonstrated that these state equations can propagate freely and accurately through time without suffering from numerical problems.

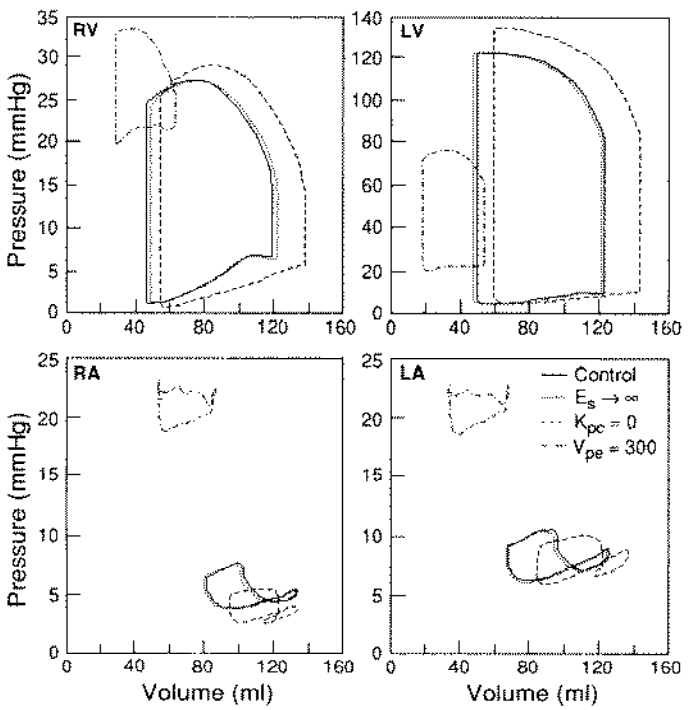

Fig. 11. Effects of removing transseptal coupling ($E_s \rightarrow \infty$), removing pericardial coupling ($K_{pc} = 0$), and cardiac tamponade ($V_{pe} = 300$ ml) on pressure-volume loops in 4 cardiac chambers. See *Glossary* for definition of abbreviations.

Although the model has been developed with a broad scope and may have many other applications, the present study is focused on the right-left heart interaction. The purpose of the model-based study is to characterize quantitatively the causal relationships between several circulatory parameters and their hemodynamic consequences and to predict the hemodynamic waveforms under various disease conditions involving the right-left heart interaction. The validity of the model is supported by *1*) its accurate representation of the baseline hemodynamics in various parts of the circulatory system, *2*) its good fit to clinically measured pressure and flow-velocity waveforms, and *3*) its correct prediction of the hemodynamic consequences in response to the changes in circulatory variables for mitral abnormalities, heart failures, cardiac tamponade, and the Valsalva maneuver. The various disease conditions are chosen not only because they involve the right-left heart interaction but also because a useful comprehensive model should stand the challenge of stretching its representation over a broad physiological range. Specific findings pertaining to the right-left heart interaction and limitations of the model are discussed as follows.

Three mechanisms are implemented in the model for the right-left heart interaction: *1*) hemodynamic coupling via the pulmonary circulation, *2*) volume coupling among the chambers in the pericardium, and *3*) pressure coupling through the interventricular septum. The present study provides simulation data to characterize the individual coupling mechanisms in a quantitative way. The transseptal coupling affects the hemodynamic indexes ≤2% (Table 4). Whereas the total heart

Table 4. *Effect of septal and pericardial coupling on hemodynamics*

	Heart Rate	Cardiac Output	Systolic p_{ao}	Diastolic p_{ao}	End-Diastolic					Mean				
					p_{rv}	p_{lv}	p_{pa}	v_{lv}	v_{lv}	p_{ra}	p_{la}	v_{pul}	v_{heart}	v_v
a) $E_s \rightarrow \infty$	−1	0	0	0	1	−2	−2	1	−2	1	−2	−1	0	0
b) $K_{pe} = 0$	−8	7	12	3	−8	6	−5	17	18	−20	−2	−1	18	−4
c) *a* + *b*	−8	9	12	4	−8	3	−7	18	17	−20	−5	−2	17	−4
d) $E_s = 20$	0	0	0	0	−1	3	3	−2	2	0	4	1	0	0

Values are expressed in percent. *a*, septal coupling removed; *b*, pericardial coupling removed; *c*, septal and pericardial coupling removed; *d*, septal coupling increased. See *Glossary* for definition of abbreviations.

volume remains unchanged, the transseptal coupling shifts a small amount of RV volume to the LV; end-diastolic p_{lv} and mean p_{la} are also slightly increased. When the transseptal coupling is increased, an additional 3% increase is observed in end-diastolic p_{lv} and p_{pa}. The direction and magnitude of these hemodynamic changes are generally in agreement with the findings by Santamore and Burkhoff (24). In contrast, the pericardial coupling has a more prominent effect on the baseline hemodynamics. The pericardial compression reduces total heart volume by 18%, cardiac output by 7%, and systolic p_{ao} by 12% and increases end-diastolic p_{rv} by 8% and mean p_{ra} by 20%. The pressure-volume loops in Fig. 11 further illustrate the instantaneous effects of transseptal and pericardial coupling on the four cardiac chambers.

The simulations of RHF and LHF show that damming of blood in the pulmonary and systemic venous reservoir is a direct hemodynamic consequence of reducing ventricular contractility. In the case of mild LHF with 50% reduction of LV contractility, mean p_{la} rises from 8.1 to 14 mmHg. This result is generally consistent with the model prediction by Burkhoff and Tyberg (2), which showed an increase in mean v_{pul} from 12 to 15 mmHg with 50% reduction of LV end-systolic elastance. In the case of severe LHF with 75% reduction of LV contractility, our model shows that mean v_{pul} and v_v increase by 42 and 19%, respectively; mean p_{la} and p_{ra} also increase drastically by 162 and 174%, respectively. These drastic changes in hemodynamics are predicted by our model without involving the mechanism of reflex-mediated decrease in vascular capacity, as suggested previously (2). The large increases in the venous pressures are attributed in part to the nonlinearity of vascular capacitances; i.e., pressure is an exponential function of vascular volume. The simulations of MS and MR further demonstrate how left heart abnormalities extend their influences to the right heart. In patients with chronic mitral abnormalities, the LA and LV elastances are often modified by enlargement and/or hypertrophy. The chronic adaptation is not considered in the present study in an attempt to isolate the hemodynamic consequences of changing a single variable, i.e., the mitral valve area.

Cardiac tamponade, a potentially fatal condition characterized by the equalization of all pressures in the cardiac chambers at end diastole, is often caused by pericardial diseases (5). The characteristic hemodynamic waveforms for cardiac tamponade are accurately predicted by the model with an increase in V_{pe} from 30 to 300 ml. As shown in Fig. 8, at end diastole all chamber pressures converge within a range of 2 mmHg. The ventricular pressures p_{rv} and p_{lv} show the pattern of early-diastolic dip followed by middiastolic plateau, typically observed in patients with cardiac tamponade (17). All flows into and out of the heart diminish during diastole, because the early-diastolic increase in v_{heart} significantly elevates the pericardial compression on all cardiac chambers.

The p_{pw} provides a unique possibility to access left heart dynamics by right-sided catheterization. In clinical situations it is practically easier to perform catheterization on the right side than on the left side of the circulation. The present model includes a special section to simulate the p_{pw}. This is accomplished by separating a small portion of the pulmonary vessels distal to the p_{pw} catheter from the rest of the pulmonary circulation. As flow into this section ceases, the pressure measured through the pulmonary capillaries and veins should reflect the LA pressure. For all simulations in this study, p_{pw} always follows p_{la}, showing the appropriate damping and delay. The p_{pw} waveforms summarized in Fig. 9 demonstrate the shapes and variations of the a wave, x descent, v wave, and y descent typically observed in the in vivo situations. In MS the absence of y descent reflects the reduced rate of transmitral flow. In MR the characteristic large v wave is predicted. In cardiac tamponade the equally elevated a and v waves, the rapid x descent, and the disappearance of y descent are accurately predicted.

The exact mechanism of pulsus paradoxus is still unclear (21). A hypothesis has been formed on the basis of leftward motions of the interventricular septum during inspiration: Inspiration increases venous return, which in turn increases right heart volume. Because of the septal and pericardial coupling, left heart volume is suppressed and systemic arterial pressure falls. Our model shows that pericardial effusion suppresses the left heart volume more than the right heart volume (higher right heart volume curves in Fig. 8 and upward shift of the RV pressure-volume loop in Fig. 11), which reflects the experimental observations by Ditchey et al. (8). However, pericardial effusion alone is not sufficient to cause pulsus paradoxus, nor does transseptal coupling contribute to the occurrence of pulsus paradoxus. The simulation of pulsus paradoxus (Fig. 10*B*) is accomplished by, in addition to inducing cardiac tamponade, changing the p_{ita} from −1.8 to −8 mmHg. The increase in p_{it} magnitude during cardiac tamponade is evidenced in the experimental data reported by Shabetai et al. (25). Intrathoracic pressure can vary over a broad range, and its

magnitude can easily be increased by a stronger breathing effort. Because acute cardiac tamponade is frequently associated with dyspnea (35), it is hypothesized on the basis of the simulation result that the increase in the p_{it} magnitude contributes in part to the occurrence of pulsus paradoxus. This hypothesis for the mechanism of pulsus paradoxus should merit further investigations.

The Valsalva maneuver, forced expiration against a closed glottis, is used clinically to differentiate murmurs, assess baroreflex function, and evaluate heart failure (11). The four phases of the Valsalva maneuver are accurately simulated by the model. The simulation is simply accomplished by holding the intrathoracic pressure to 40 mmHg during a 10-s period. In contrast, the hemodynamic consequences as shown by the p_{ao} waveform in Fig. 10*C* are quite complex and involve several mechanisms. After the transient rise (*phase 1*), the increased pressure in the cardiovascular system quickly dissipates. This can be explained by, referring to the electrical analog in Fig. 1, the fact that p_{it} is coupled to the cardiovascular system through vascular and chamber capacitances. The ability of these capacitances to absorb the intrathoracic pressure depends on how effectively they can redistribute blood volumes in the compliant chambers and vessels. The arterial pressure continues to decline below the normal level, because the venous return is held back and the pulmonary reservoir is gradually depleted by the elevated intrathoracic pressure (*phase 2*). The baroreflex causes heart rate to increase, from 70 beats/min (control) to 86 beats/min in our simulation. The release of the intrathoracic pressure causes the transient increase (*phase 3*), which again is quickly absorbed by the cardiovascular capacitances. After the release, arterial pressure increases above the normal level as a result of the surge from the retained venous return. The baroreflex causes heart rate to decrease to 61 beats/min (*phase 4*). In vivo data sometimes showed even higher arterial pressure elevation and more prominent bradycardia during *phase 4* (11). This may be attributed to the baroreflex-mediated increase in arterial resistance, which is not included in the present model.

Although the present model with its 74 elements may seem rather complex, the model representation has been simplified as much as possible during the model development process. The degree of complexity is dictated by the number of various compartments essential to the model representation. For the purpose of studying the right-left heart interaction, some compartments may be less significant than others. For example, the coronary circulation could have been excluded, because the coronary flow accounts for <5% of the cardiac output. However, we chose to include the coronary model, because it is readily available from a previous study (33) and should be useful for future research involving coronary-ventricular interaction. The section for p_{pw} also contributes little to the overall hemodynamics. This section is included because of our interest in assessing left-sided dynamics with right-sided catheterization, as discussed above.

We chose a four-element basic model for each compartment: *R*, *L*, capacitance, and Ω. Many other models (1, 15, 24) exclude *L* and/or Ω, which is probably justified by their relatively small contribution to the overall hemodynamics. The sensitivity analysis in this study also confirms that the *R*, *L*, and Ω are relatively insensitive. However, these parameters are important for generating the correct shapes of pressure and flow waveforms in the local compartments. The nonlinear resistance governed by Bernoulli's law is important for the dynamics of the heart valves. The nonlinear vascular capacitance, especially in low-pressure veins and capillaries, is important for characterizing the hemodynamic aspect of the right-left heart interaction. Although it is difficult to prove the uniqueness of the model representation for a given hemodynamic condition, each model parameter is associated with a well-defined hemodynamic consequence, and we have never experienced any problem with ambiguity in adjusting the model parameters. The results of sensitivity analysis summarized in Table 3 also provide a valuable guideline for tuning the model parameters to a certain physiological condition.

The present model does not represent the entire cardiovascular system. As shown by the volume distributions in Table 1, the systemic arteries and veins are only partially represented; the systemic capillaries are completely excluded in the model. Because of the distributive nature of the systemic peripheral circulation, this omission should have only minimal effects on the central circulation. The arteriovenous coupling is significantly simplified by adjusting $\dot{Q}_v$ in a semiautomatic way. For the simulation of the disease conditions, $\dot{Q}_v$ was set equal to the cardiac output at the point when the simulation ran continuously for 50 cardiac cycles after the change of a model parameter. Because the systemic venous reservoir is about six to seven times larger than the total pulmonary reservoir, the change in venous return caused by the imbalance between $\dot{Q}_v$ and the present cardiac output occurs very gradually. As shown in Fig. 5, cardiac output is mainly controlled by the intrinsic condition of the heart and is relatively insensitive to $\dot{Q}_v$. The choice of $\dot{Q}_v$ determines the volume of the venous reservoir and the preload pressure. Setting $\dot{Q}_v$ in our model is analogous to the preload management for cardiac patients, i.e., to adjust the operating point along a Starling curve (cardiac output vs. venous pressure) by controlling the patient's fluid volume. Appropriate modeling of the arteriovenous interaction must include the complex mechanisms for neurohumoral regulation and fluid exchanges with the lymphatic system and interstitial space (13). We chose not to close the loop in the present circulatory model, because the development of the arteriovenous model would require much more work and is beyond the scope of the present study.

Limitations of the model. Baroreflex control of heart rate is represented in the model by use of a simple first-order relationship between the cardiac period and the systolic p_{ao}. Although this simplified mechanism seems effective to predict the changes in heart rate for the various disease conditions under investigation, the

neurohormonal control of cardiovascular dynamics (13) is far more sophisticated than that considered in the present model. This limitation may affect the simulations of pulsus paradoxus and the bradycardia phase of the Valsalva maneuver. Another limitation is concerned with the lumped-parameter representation of the pulmonary circulation. Although the total volume of the pulmonary circulation is accurately represented in the model, the distribution of blood among the pulmonary arteries, capillaries, and veins does not match exactly the in vivo data (Table 1). The phenomenon of pressure wave propagation in the pulmonary circulation cannot be characterized in the present model. This limitation may be related to the minor discrepancy between measured and model-fitted p_{pa} during diastole (Fig. 3), which can be explained by the lack of reflection waves in the lumped-parameter model. To represent the wave propagation would require a model of much higher order, as shown by Pollack et al. (22).

Conclusions. A mathematical model has been developed to characterize the right-left heart interaction with a broad spectrum of hemodynamic waveforms for normal and pathological physiology. The model predicts various characteristic changes in pressure and flow waveforms as direct hemodynamic consequences. The pericardial coupling has a significant effect (up to 20%) and the transseptal coupling has a minor effect (up to 2%) on baseline hemodynamics. Accurate simulations are demonstrated in fitting clinical pressure and Doppler-echocardiographic data and in characterizing MS, MR, LHF, RHF, cardiac tamponade, pulsus paradoxus, and the Valsalva maneuver. The model-based simulation should be useful for quantitative studies of cardiopulmonary dynamics. The model, with its comprehensive, phenomenological, and versatile nature, should also be useful for tutorial purposes. As a direction for future research the model can provide a platform to integrate more sophisticated mechanisms for neurohormonal regulation of the cardiovascular dynamics.

APPENDIX

The dynamics of the model shown in Fig. 1 are completely characterized by the following 28 state equations

$$\frac{dv_v}{dt} = \dot{Q}_v - \dot{q}_v \tag{A1}$$

$$\frac{d\dot{q}_v}{dt} = \left(E_v\Phi_v - R_v\dot{q}_v - E_{vc}\Phi_{vc} + \Omega_v\frac{dv_v}{dt} - \Omega_{vc}\frac{dv_{vc}}{dt} - P_{it}\right)\Big/L_v \tag{A2}$$

$$\frac{dv_{vc}}{dt} = \dot{q}_v - \dot{q}_{vc} \tag{A3}$$

$$\frac{d\dot{q}_{vc}}{dt} = \left(E_{vc}\Phi_{vc} - e_{ra}v_{ra} - R_{vc}\dot{q}_{vc} + \Omega_{vc}\frac{dv_{vc}}{dt} - \Omega_{ra}\frac{dv_{ra}}{dt} - p_{pc}\right)\Big/L_{vc} \tag{A4}$$

$$\frac{dv_{ra}}{dt} = \dot{q}_{vc} + \dot{q}_{co} - \dot{q}_{tv} \tag{A5}$$

$$\frac{d\dot{q}_{tv}}{dt} = \begin{cases} \left(e_{ra}v_{ra} - \hat{e}_{rv}v_{rv} - k_{lr}p_{lv} - R_{tv}\dot{q}_{tv} - b_{tv}\dot{q}_{tv}|\dot{q}_{tv}| + \Omega_{ra}\dfrac{dv_{ra}}{dt} - \Omega_{rv}\dfrac{dv_{rv}}{dt}\right)\Big/L_{tv} & A_{tv} > 0 \\ 0 & \text{otherwise} \end{cases} \tag{A6}$$

$$\frac{dv_{rv}}{dt} = \dot{q}_{tv} - \dot{q}_{pv} \tag{A7}$$

$$\frac{d\dot{q}_{pv}}{dt} = \begin{cases} \left(\hat{e}_{rv}v_{rv} + k_{lr}p_{lv} - E_{pua}\Phi_{pua} - R_{pv}\dot{q}_{pv} - b_{pv}\dot{q}_{pv}|\dot{q}_{pv}| + \Omega_{rv}\dfrac{dv_{rv}}{dt} - \Omega_{pua}\dfrac{dv_{pua}}{dt} + p_{pc}\right)\Big/L_{pv} & A_{pv} > 0 \\ 0 & \text{otherwise} \end{cases} \tag{A8}$$

$$\frac{dv_{pua}}{dt} = \dot{q}_{pv} - \dot{q}_{pua} - \dot{q}_{pwa} \tag{A9}$$

$$\frac{d\dot{q}_{pua}}{dt} = \left(E_{pua}\Phi_{pua} - E_{puc}\Phi_{puc} - R_{pua}\dot{q}_{pua} + \Omega_{pua}\frac{dv_{pua}}{dt} - \Omega_{puc}\frac{dv_{puc}}{dt}\right)\Big/L_{pua} \tag{A10}$$

$$\frac{dv_{puc}}{dt} = \dot{q}_{pua} - \dot{q}_{puc} \tag{A11}$$

$$\frac{d\dot{q}_{puc}}{dt} = \left(E_{puc}\Phi_{puc} - E_{puv}\Phi_{puv} - R_{puc}\dot{q}_{puc} + \Omega_{puc}\frac{dv_{puc}}{dt} - \Omega_{puv}\frac{dv_{puv}}{dt}\right)\Big/L_{puc} \tag{A12}$$

$$\frac{dv_{puv}}{dt} = \dot{q}_{puc} - \dot{q}_{puv} \tag{A13}$$

$$\frac{d\dot{q}_{puv}}{dt} = \left(E_{puv}\Phi_{puv} - e_{la}v_{la} - R_{puv}\dot{q}_{puv} + \Omega_{puv}\frac{dv_{puv}}{dt} - \Omega_{la}\frac{dv_{la}}{dt} - p_{pc}\right)\Big/L_{puv} \tag{A14}$$

$$\frac{d\dot{q}_{pwa}}{dt} = \begin{cases} \left(E_{pua}\Phi_{pua} - E_{pwc}\Phi_{pwc} - \dot{q}_{pwa}/g_{pw} + \Omega_{pua}\dfrac{dv_{pua}}{dt} - \Omega_{pwc}\dfrac{dv_{pwc}}{dt}\right)\Big/L_{pwa} & \text{if } g_{pw} > 0 \\ 0 & \text{otherwise} \end{cases} \tag{A15}$$

$$\frac{dv_{pwc}}{dt} = \dot{q}_{pwa} - \dot{q}_{pwc} \tag{A16}$$

$$\frac{d\dot{q}_{pwc}}{dt} = \left(E_{pwc}\Phi_{pwc} - E_{pwv}\Phi_{pwv} - R_{pwc}\dot{q}_{pwc} + \Omega_{pwc}\frac{dv_{pwc}}{dt} - \Omega_{pwv}\frac{dv_{pwv}}{dt}\right)\Big/ L_{pwc} \quad (A17)$$

$$\frac{dv_{pwv}}{dt} = \dot{q}_{pwc} - \dot{q}_{pwv} \quad (A18)$$

$$\frac{d\dot{q}_{pwv}}{dt} = \left(E_{pwv}\Phi_{pwv} - e_{la}v_{la} - R_{pwv}\dot{q}_{pwv} + \Omega_{pwv}\frac{dv_{pwv}}{dt} - \Omega_{la}\frac{dv_{la}}{dt} - p_{pc}\right)\Big/ L_{pwv} \quad (A19)$$

$$\frac{dv_{la}}{dt} = \dot{q}_{puv} + \dot{q}_{pwv} - \dot{q}_{mv} \quad (A20)$$

$$\frac{d\dot{q}_{mv}}{dt} = \begin{cases} \left(e_{la}v_{la} - \hat{e}_{lv}v_{lv} - k_{rl}p_{rv} - R_{mv}\dot{q}_{mv} - b_{mv}\dot{q}_{mv}|\dot{q}_{mv}| + \Omega_{la}\dfrac{dv_{la}}{dt} - \Omega_{lv}\dfrac{dv_{lv}}{dt}\right)\Big/ L_{mv} & A_{mv} > 0 \\ 0 & \text{otherwise} \end{cases} \quad (A21)$$

$$\frac{dv_{lv}}{dt} = \dot{q}_{mv} - \dot{q}_{av} \quad (A22)$$

$$\frac{d\dot{q}_{av}}{dt} = \begin{cases} \left(\hat{e}_{lv}v_{lv} + k_{rl}p_{rv} - E_{aa}\Phi_{aa} - R_{av}\dot{q}_{av} - b_{av}\dot{q}_{av}|\dot{q}_{av}| + \Omega_{lv}\dfrac{dv_{lv}}{dt} - \Omega_{aa}\dfrac{dv_{aa}}{dt} + p_{pc}\right)\Big/ L_{av} & A_{av} > 0 \\ 0 & \text{otherwise} \end{cases} \quad (A23)$$

$$\frac{dv_{aa}}{dt} = \dot{q}_{av} - \dot{q}_{aa} - \dot{q}_{co} \quad (A24)$$

$$\frac{d\dot{q}_{aa}}{dt} = \left(E_{aa}\Phi_{aa} - E_{da}\Phi_{da} - R_{aa}\dot{q}_{aa} + \Omega_{aa}\frac{dv_{aa}}{dt} - \Omega_{da}\frac{dv_{da}}{dt}\right)\Big/ L_{aa} \quad (A25)$$

$$\frac{dv_{da}}{dt} = [R_{ca}(\dot{q}_{aa} - \dot{q}_{da}) - E_{da}\Phi_{da} - P_{it}]/(\Omega_{da} + R_{ca}) \quad (A26)$$

$$\frac{d\dot{q}_{da}}{dt} = \left(E_{da}\Phi_{da} - E_{a}\Phi_{a} - R_{da}\dot{q}_{da} + \Omega_{da}\frac{dv_{da}}{dt} - \Omega_{a}\frac{dv_{a}}{dt} + P_{it}\right)\Big/ L_{da} \quad (A27)$$

$$\frac{dv_{a}}{dt} = (R_{a}\dot{q}_{da} - E_{a}\Phi_{a})/(\Omega_{a} + R_{a}) \quad (A28)$$

To demonstrate how the state equations are derived, the derivation of the first two state equations is given as follows.

At *node 1* in Fig. 1 the continuity of flows requires

$$\dot{Q}_{v} = \frac{dv_{v}}{dt} + \dot{q}_{v}$$

where $\dot{Q}_{v}$ is the flow into *node 1*, dv_{v}/dt is the flow from *node 1* to the venous reservoir represented by E_{v}, and $\dot{q}_{v}$ is the flow from *node 1* to L_{v}. By rearranging terms in the above equation with the derivative term on the left-hand side, we obtain state *Eq. A1*.

At *node 2* we have

$$\dot{q}_{v} = \left(E_{v}\Phi_{v} + \Omega_{v}\frac{dv_{v}}{dt} + L_{v}\frac{d\dot{q}_{v}}{dt} - E_{vc}\Phi_{vc} - \Omega_{vc}\frac{dv_{vc}}{dt} - P_{it}\right)\Big/ R_{v}$$

where the right-hand side is the flow through R_{v} computed as the pressure gradient divided by the resistance. By extracting $d\dot{q}_{v}/dt$ to the left-hand side, we obtain state *Eq. A2*.

The rest of the state equations can be derived in a similar way. Notice that some equations are dependent on others. For example, *Eq. A2* has two derivative terms on its right-hand side that must be first determined by *Eqs. A1* and *A3*. To resolve the dependency among the equations at each step of the numerical integration, the independent equations are evaluated before the dependent equations. There are 14 independent equations, i.e., *Eqs. A1, A3, A5, A7, A9, A11, A13, A16, A18, A20, A22, A24, A26,* and *A28*; the other 14 equations are dependent.

Address for reprint requests: Y. Sun, Dept. of Electrical and Computer Engineering, University of Rhode Island, Kingston, RI 02881.

Received 22 January 1996; accepted in final form 12 September 1996.

REFERENCES

1. **Beyar, R., M. J. Hausknecht, H. R. Halperin, F. C. P. Yin, and M. L. Weishfeldt.** Interaction between cardiac chambers and thoracic pressure in intact circulation. *Am. J. Physiol.* 253 (*Heart Circ. Physiol.* 22): H1240–H1252, 1987.
2. **Burkhoff, D., and J. V. Tyberg.** Why does pulmonary venous pressure rise after onset of LV dysfunction: a theoretical analysis. *Am. J. Physiol.* 265 (*Heart Circ. Physiol.* 34): H1819–H1828, 1993.
3. **Braunwald, E., and W. Grossman.** Clinical aspects of heart failure. In: *Heart Disease*, edited by E. Braunwald. Philadelphia, PA: Saunders, 1992, p. 444–463.
4. **Braunwald, E., E. H. Sonnenblick, and J. Ross.** Mechanisms of cardiac contraction and relaxation. In: *Heart Disease*, edited by E. Braunwald. Philadelphia, PA: Saunders, 1992, p. 351–392.
5. **Cohen, M. L.** Experimental cardiac tamponade: correlation of pressure, flow velocity, and echocardiographic changes. *J. Appl. Physiol.* 69: 924–931, 1990.
6. **Cornish, K. G., M. W. Barazanji, T. Yong, and J. P. Gilmore.** Volume expansion attenuates baroreflex sensitivity in the conscious nonhuman primates. *Am. J. Physiol.* 257 (*Regulatory Integrative Comp. Physiol.* 26): R595–R598, 1989.
7. **Dahn, I., B. Jonson, and R. Nilsén.** Plethysmographic in vivo determinations of elastic properties of arteries in man. *J. Appl. Physiol.* 28: 328–332, 1970.

8. **Ditchey, R., R. Engler, M. LeWinter, R. Palvelec, V. Bhargava, J. Covell, W. Moores, and R. Shabetai.** The role of the right heart in acute cardiac tamponade in dogs. *Circ. Res.* 48: 701–710, 1981.
9. **Engelberg, J., and A. B. DuBois.** Mechanics of pulmonary circulation in isolated rabbit lungs. *Am. J. Physiol.* 196: 401–414, 1959.
10. **Freeman, G. L., and M. M. LeWinter.** Pericardial adaptations during chronic cardiac dilation in dogs. *Circ. Res.* 54: 294–300, 1984.
11. **Gorlin, R., J. H. Knowles, and C. F. Storey.** The Valsalva maneuver as a test of cardiac function: pathologic physiology and clinical significance. *Am. J. Med.* 22: 197–212, 1957.
12. **Guyton, A. C.** *Textbook of Medical Physiology* (8th ed.). Philadelphia, PA: Saunders, 1992, p. 150–254.
13. **Guyton, A. C., T. G. Coleman, and H. J. Granger.** Circulation: overall regulation. *Annu. Rev. Physiol.* 34: 13–46, 1972.
14. **Hardy, H. H., and R. E. Collins.** On the pressure-volume relationship in circulatory elements. *Med. Biol. Eng. Comput.* 20: 565–570, 1982.
15. **Hardy, H. H., R. E. Collins, and R. E. Calvert.** A digital computer model of the human circulatory system. *Med. Biol. Eng. Comput.* 20: 550–564, 1982.
16. **Hope, J. A.** *Treatise on the Diseases of the Heart and Great Vessels.* London: Williams-Kidd, 1832.
17. **Kern, M. J.** *The Cardiac Catheterization Handbook.* New York: Mosby-Year Book, 1991, p. 147–171.
18. **Lau, V.-K., and K. Sagawa.** Model analysis of the contribution of atrial contraction to ventricular filling. *Ann. Biomed. Eng.* 7: 167–201, 1979.
19. **Mackenzie, J.** *Disease of the Heart* (3rd ed.). London: Oxford University Press, 1913.
20. **Maughan, W. L., K. Sunagawa, and K. Sagawa.** Ventricular systolic interdependence: volume elastance model in isolated canine hearts. *Am. J. Physiol.* 253 (*Heart Circ. Physiol.* 22): H1381–H1389, 1987.
21. **McGregor, M.** Pulsus paradoxus. *N. Engl. J. Med.* 301: 480–482, 1979.
22. **Pollack, G. H., R. V. Reddy, and A. Noordergraaf.** Input impedance, wave travel, and reflections in the human pulmonary arterial tree: studies using an electrical analog. *IEEE Trans. Biomed. Eng.* 15: 151–164, 1968.
23. **Robinson, B. F.** Relation of heart rate and systolic pressure to the onset of pain in angina pectoris. *Circulation* 35: 1073–1083, 1967.
24. **Santamore, W. R., and D. Burkhoff.** Hemodynamic consequences of ventricular interaction as assessed by model analysis. *Am. J. Physiol.* 260 (*Heart Circ. Physiol.* 29): H146–H157, 1991.
25. **Shabetai, R., N. O. Fowler, J. C. Fenton, and M. Masangkay.** Pulsus paradoxus. *J. Clin. Invest.* 44: 1882–1898, 1965.
26. **Shoukas, A. A.** Pressure-flow and pressure-volume relations in the entire pulmonary vascular bed of the dog determined by two-port analysis. *Circ. Res.* 37: 809–818, 1975.
27. **Shroff, S. G., J. S. Janicki, and K. T. Weber.** Evidence and quantitation of left ventricular systolic resistance. *Am. J. Physiol.* 249 (*Heart Circ. Physiol.* 18): H358–H370, 1985.
28. **Slinker, B. K., and S. A. Glantz.** End-systolic and end-diastolic ventricular interaction. *Am. J. Physiol.* 251 (*Heart Circ. Physiol.* 20): H1062–H1075, 1986.
29. **Snyder, M. F., V. C. Rideout, and R. J. Hillestad.** Computer modeling of the human systemic arterial tree. *IEEE Trans. Biomed. Eng.* 14: 171–177, 1967.
30. **Suga, H., and K. Sagawa.** Theoretical analysis of a left-ventricular pumping model based on the systolic time-varying pressure volume ratio. *IEEE Trans. Biomed. Eng.* 18: 47–55, 1971.
31. **Sun, Y.** Modeling the dynamic interaction between left ventricle and intra-aortic balloon pump. *Am. J. Physiol.* 261 (*Heart Circ. Physiol.* 30): H1300–H1311, 1991.
32. **Sun, Y., and S. A. Chiaramida.** Simulation of hemodynamics and regulatory mechanisms in the cardiovascular system based on a nonlinear and time-varying model. *Simulation* 59: 28–36, 1992.
33. **Sun, Y., and H. Gewirtz.** Estimation of intramyocardial pressure and coronary blood flow distribution. *Am. J. Physiol.* 255 (*Heart Circ. Physiol.* 24): H664–H672, 1988.
34. **Sun, Y., B. Janerot-Sjöberg, P. Ask, D. Loyd, and B. Wranne.** Mathematical model that characterizes transmitral and pulmonary venous flow velocity patterns. *Am. J. Physiol.* 268 (*Heart Circ. Physiol.* 37): H476–H489, 1995.
35. **Symmes, J. C., and N. D. Berman.** Early recognition of cardiac tamponade. *Can. Med. Assoc. J.* 116: 863–864, 1977.
36. **Taylor, R. R., J. W. Covell, E. H. Sonnenblick, and J. Ross, Jr.** Dependence of ventricular distensibility of filling the opposite ventricle. *Am. J. Physiol.* 213: 711–718, 1967.